



**An individual based computational model of intestinal crypt fission and its application to predicting unrestricted growth of the intestinal epithelium**

Journal:	<i>Integrative Biology</i>
Manuscript ID:	Draft
Article Type:	Paper
Date Submitted by the Author:	n/a
Complete List of Authors:	pin, carmen; institute of Food Research, Parker, Aimee; Institute of Food Research, Gut Health Food Safety gunning, allan; institute of food research, food and health Ohta, Yuki; Keio University, School of Medicine Johnson, Ian; Institute of Food Research, Carding, Simon; Institute of Food Research, Sato, Toshiro; Keio Univeristy,
<p>Note: The following files were submitted by the author for peer review, but cannot be converted to PDF. You must view these files (e.g. movies) online.</p>	
<p>Supplementary_Video S1.qt Supplementary_Video S2.qt</p>	



Institute of Food Research  
Norwich Research Park  
Colney  
Norwich NR4 7UA  
UK  
[www.ifr.ac.uk](http://www.ifr.ac.uk)

Norwich, 10 March 2014

Intestinal crypt fission is a homeostatic phenomenon, observed rarely in healthy adult mucosa, which also plays a pathological role as the main mode of growth of intestinal polyps. Difficulties in observing experimentally crypt fission has limited its understanding. Recently developed experimental techniques have been integrated with theoretical models in order to gain novel insights into this process. An agent based model has been combined with measurements from *in vitro* culturing intestinal organoids to develop an innovative computational approach able to simulate the process of crypt fission and further to extrapolate predictions for the growth of adenomatous polyps in the intestinal epithelium.

The Institute of Food Research is a registered charity (No. 1058499)  
and a company limited by guarantee (registered in England and Wales No. 03009972).  
VAT registration No. GB 688 8914 52

IFR receives strategic funding from the Biotechnology and Biological Sciences Research Council

Monday, 16 October 2014

Dear Dr Barcellos-Hoff:

**Revised version of Manuscript ID IB-ART-03-2014-000055**

**Title: An individual based computational model of intestinal crypt fission and its application to predicting unrestrictive growth of the intestinal epithelium**

We are very thankful for the opportunity of revising and resubmitting our manuscript and for the extra time given to address all reviewers' concerns.

We would like to thank the referees for their constructive comments and wise suggestions that in our opinion have contributed to strengthen the work presented here. As suggested, we have carried out additional experiments in order to verify the position of stem and Paneth cells in the organoids (point 2 reviewer 1) and to measure the biomechanical properties of stem and Paneth cells by Atomic Force Microscopy (AFM) in order to support our hypothesis with experimental evidences (Point 1 reviewer 2 and general concern of reviewer2). The generation of new data involving experiments with LGr5+ GFP mice, fluorescent labelling and imaging of grown organoids and AFM measurements were the reason for the extra time required to prepare this revised version.

The generation of new data also involved the addition of new co-authors in this paper: Yuki Ohta carried out the fluorescent labelling and imaging of stem and Paneth cells in organoids generated from Lgr5+ mice crypts at Keio University; Aimee Parker and A. Patrick Gunning carried out AFM measurements on stem and Paneth cells isolated from Lgr5+ mice crypts at the institute of Food Research.

We would be glad if you could consider the revised version of this manuscript for publication in the journal Integrative Biology. A point by point reply to the reviewers' comments is attached below.

Best regards  
Carmen Pin

**Reviewer(s)' Comments to Author:**

**Referee: 1**

**Comments to the Author**

**The article propose a very interesting and innovative theory, according to which the process of crypt fission is driven by a difference between the biomechanical properties of Paneth cells respect to stem cells.**

**This hypothesis is confirmed by the agreement between the computational model (built on the mentioned hypothesis) and the dynamics observed in an in vitro organoid model. The computational model looks complete and detailed. The fluid mechanic approach is innovative.**

**Nevertheless, there is no evidence that the claimed difference in biomechanical properties could be true, nor in vivo nor in vitro.**

Response. We have measured mechanical properties of Lgr5+ stem cells and of non-fluorescent cells. Results explained below in response to question 1.

**Also, it is not clear in the method how the difference in biomechanical properties is set in the computational model (a "force" is compared to a "size").**

Response. The Model section has been rewritten and forces definition and all estimations clarified. See "Biomechanical model for the initiation of buds" in the Material and Methods section of the revised version of the paper

**In my opinion, to be a reliable hypothesis there is the need of:**

**1) Experimental data on the biomechanical properties of paneth and stem cells (i.e., by atomic force microscopy).**

We have measured the Young modulus of Lgr5+ stem cells and of non-fluorescent cells by AFM. Results are shown in Figure 3. The following paragraph has been added to the results

*"In order to support this hypothesis, Atomic Force Microscopy (AFM) has been used to measure the Young modulus of Lgr5-eGFP positive cells and Lgr5-eGFP negative large granular crypt cells. The Young modulus is a measure of stiffness that quantifies the linear stress-strain relationship in the range of stress where Hook's law holds. Figure 3A shows that the Young modulus of all but one of the Lgr5-eGFP positive cells was significantly smaller than that of large granular cells by more than 3 times the standard deviation. Lgr5-eGFP positive cells, which were assumed to be stem cells, required significantly smaller forces to undergo deformation than large granular cells, which were assumed to be Paneth cells. Moreover, we have assumed that cells behave as viscous materials rather than the solid material behaviour described in previous models. Viscoelastic behaviour of cells was demonstrated in force curves. AFM measurements showed the typical separation, or hysteresis, between the approach and retract force curves resulting from viscous behaviour in all assessed cells (Figure 3B)."*

**2) Fluorescent labeling and imaging of paneth cells and stem cells on the organoids to verify their positions.**

Fluorescent labelling and imaging of Paneth cells and stem cells on the organoids has been carried out and it is shown in Figure 1.

The following paragraph has been added to the manuscript:

*"In mouse intestinal organoid cultures, bud formation takes place initially in regions of the primary cyst with high Paneth cell density; initial buds grow into crypts which contain Paneth and stem cells intermingling at their bases (Figure 1)."*

**3) Sensibility analysis on the parameters of the computational model, in particular on the value of the threshold "C", which has to be related to biologically relevant values of Young modulus.**

Sensitivity analysis has been carried out for the shear stress threshold in Paneth cells. Results are presented in Figure 4 are described in the following paragraph:

*"Figure 4A compares the time intervals between successive budding events observed in vitro with the intervals simulated using several values for the parameter  $\alpha$ . This parameter governs the force threshold required for Paneth cell deformation. When  $\alpha=0$ , Paneth cells*

*have identical mechanical properties to stem cells. When  $\alpha=1$ , the force required to deform Paneth cells is equal to the force generated by a disequilibrium between available and required space equal to one average cell size; if  $\alpha$  is smaller or greater than 1, Paneth cell deformation requires forces smaller or greater, respectively, than that generated by one extra cell. When crypts were simulated with  $\alpha=0$  and  $\alpha=0.1$ , Paneth cells were deformed, and changes in cell size were translated in the flow of cell contents from crypt bottom to top without deformations of the crypt wall. This unimpeded flow was due to the non-stress boundary at the top of the crypt because of unrestrictive cell removal. As the value of  $\alpha$  increased, Paneth cells became more resistant to deformation so that the increase in size and/or decrease of available space during the cell cycle was not accommodated by the non-deformable neighbouring Paneth cells, leading to protrusion of cell material out of the crypt wall and bud formation. In simulated crypts, the frequency of budding increased rapidly as the value of  $\alpha$  increased from 0 to 1. The best agreement between simulated and observed distributions of frequencies for the time interval between successive budding events was observed for values of  $\alpha$  slightly greater than 1. For instance, the smallest difference between the simulated and observed distribution was detected for  $\alpha=1.3$  (Figure 4B)."*

## **Referee: 2**

### **Comments to the Author**

**I found the individual based model of intestinal crypt fission to be quite interesting.**

**However, below are suggestions for improvement.**

**The major weakness of the manuscript is that there is no experimental evidence to support their hypothesis underlying bud initiation, which is that bud initiation results from a difference in the biomechanical behavior of neighboring Paneth and stem cells.**

**However, this is now a prediction from their model since it led to simulation results that matched experimental data at various levels. The manuscript would benefit significantly if they were able to validate this prediction, especially since this prediction is presented very early on in the manuscript and it sets the foundation for the rest of the experiments.**

**Without this, it's unclear exactly what biological insights are gained from the current state of the model and the simulation results. There isn't a strong enough argument presented against modeling fission as a buckling process alone to support this new hypothesis.**

We agree with the referee that the novelty of our work is showing an alternative mechanism for crypt fission based on differences on the mechanical features of stem and Paneth cells. To support experimentally our main hypothesis that Paneth cells are more resistant to deformation than Stem cells, we have measured the Young's modulus of Lgr5+ stem cells and of non-fluorescent cells by AFM. Results are shown in Figure 3 and the following paragraph has been added to the results:

*"In order to support this hypothesis, Atomic Force Microscopy (AFM) has been used to measure the Young modulus of Lgr5-eGFP positive cells and Lgr5-eGFP negative large granular crypt cells. The Young modulus is a measure of stiffness that quantifies the linear stress-strain relationship in the range of stress where Hook's law holds. Figure 3A shows that the Young modulus of all but one of the Lgr5-eGFP positive cells was significantly smaller than that of large granular cells by more than 3 times the standard deviation. Lgr5-eGFP positive cells, which were assumed to be stem cells, required significantly smaller forces to undergo deformation than large granular cells, which were assumed to be Paneth cells. Moreover, we have assumed that cells behave as viscous materials rather than the solid material behaviour described in previous models. Viscoelastic behaviour of cells was*

*demonstrated in force curves. AFM measurements showed the typical separation, or hysteresis, between the approach and retract force curves resulting from viscous behaviour in all assessed cells (Figure 3B). “*

We are proposing an alternative mechanism for crypt fission and we show that it is feasible by multiple validations between observed and simulated results. We model the epithelium as formed by individual viscous cells with different properties instead of as a solid beam/layer. The immediate improvement in our approach is that cells are treated as viscous materials, which is what they are according to physical measurements; moreover in this revised version we present some evidence of the different biomechanical properties between stem cells and non-stem cells.

In addition, it could also be pointed out that previous studies modelling fission as a buckling process have been mainly theoretical articles with no experimental evidence supporting the solid mechanical behaviour of the epithelium, and very few –if any- comparisons between predictions and observations.

**“(Figure 2E)” should be changed to “(Figure 2D)”**

This has been corrected in the revised version of the manuscript. All figures are renumbered in the revised manuscript and Figure 2E is now Figure 4H which was the previous Figure 2D.

**I felt that many details of the model were missing and should be included in supplementary. How many simulations were performed? With a monte carlo simulation, each will lead to a different result. From Fig 3 legend, it looks like 89 simulations were performed. Were the same 89 simulations used to create all of the results?**

New simulations have been run in order to carry out a detailed analysis of the effect of the value of shear stress threshold of Paneth cells on model predictions. Fig 3 is now Fig 4, which merges previous Figs 2 and 3, and presents the comparison between fission measurements in simulated crypts and in cultured organoids. To do this, 30-40 crypts were simulated for 12 days, which matches the observation period in vitro, for each tested value of  $\alpha$ . Twelve values were tested.

This is clarified in Figure 4 –former Fig 3- legend as follows

**“Figure 4. Comparison between fission measurements in simulated crypts and in cultured organoids: (A) Observed (black bars; n=22 initial crypts) and simulated (red bars; n=30-40 initial crypts simulated during 12 days for each tested value of  $\alpha$ ) distributions for the time interval between successive budding processes per crypt. Plots show the results obtained with twelve values of the parameter  $\alpha$ , from 0.1 to 2, which controls the force required to deform Paneth cells”**

**It is interesting that their model can recapitulate many features observed in vitro. For example, (1) time interval between consecutive budding events, (2) crypt growth rates, and (3) positioning of the secondary crypts. Hopefully, these results are from simulations using the same model parameter values. A table of the final parameter values used should be provided in supplementary. Are any of these parameters based on biological data.**

Supplementary Table 1 with all parameters used in the simulations is provided in the revised manuscript. All simulations were run with the values presented in the Table, which are based on biological data.

As pointed out by the referee, many features observed in the simulations recapitulate observations in vivo. This is in part due to the fact that the value of the parameters of the individual based model has been chosen to minimize the error between predictions and

observations. For instance,  $\alpha=1.3$  minimize the error between the observed and simulated time interval between consecutive budding events.

In other cases, the good agreement between simulated and observed results indicates that hypotheses behind the individual based model are sufficient to describe crypt behaviour during fission. For example, the good agreement between the growth rates of the secondary crypt in simulated and in observed fission events indicates that the elongation of the secondary crypt is can be explained by cell proliferation which takes place at the same rate as in the primary crypt. The close agreement between simulated and observed migration rates of the secondary crypt shows that forces derived from cell growth and division in the primary crypt are sufficient to explain the upward migration of the secondary crypt along the primary crypt.

This is now clarified in the text.

**I question whether other computational models that simulate fission as a buckling process can also recapitulate these same features given the right parameter combination.**

Yes, it is possible.

Agreement between predictions and observations is necessary but not sufficient for model evaluation.

The essential difference between our approach and previous approaches, assuming a “solid beam” is that in those, cells are modelled as solid materials, whereas we treat them as viscous materials. AFM measurements confirmed the viscous nature of both LGR5-eGFP positive cells and large granular non-fluorescent cells isolated from crypts (Figure 3B). This indicates that our model is correct.

**page 3 “became” should be “become”**

Corrected in the new version of the manuscript.

**In the discussion, the authors state that a distinctive feature of their model is that they do not model the process as the folding or buckling of a solid material like others before. Instead, fission results from modeling the fluid mechanics at the individual cell level. This feature should be emphasized more in the manuscript as it is a key advantage of the other models.**

We have modified the following section to emphasize this point:

*“A distinctive feature of our approach to modelling crypt fission is that we treat cells as viscous materials rather than assuming the solid material behaviour described in the models discussed above. In agreement with in vitro experimental observations, we have modelled fission as a budding process based on fluid mechanics at the individual cell level and not, as the folding or buckling of solid material. AFM measurements confirmed the viscous nature of both LGR5-eGFP positive and LGR5-eGFP negative large and granular single cells isolated from crypts (Figure 3B). Moreover, we modelled fission as a consequence of inequalities in the mechanical properties of viscoelastic cells which depend on cell lineage. This hypothesis was also supported experimentally by AFM measurements of single cells, which revealed that stem cells are less stiff than other granular large crypt cells.”*

1 **An individual based computational model of intestinal crypt fission**  
2 **and its application to predicting unrestrictive growth of the intestinal**  
3 **epithelium**

4

5 Carmen Pin<sup>1\*</sup>, Aimee Parker<sup>1</sup>, A. Patrick Gunning<sup>2</sup>, Yuki Ohta<sup>3</sup>, Ian T. Johnson<sup>2</sup>,  
6 Simon R. Carding<sup>1,4</sup> and Toshiro Sato<sup>3</sup>

7

8 <sup>1</sup>Gut Health and Food Safety Research Programme, <sup>2</sup>Food and Health Research  
9 Programme, Institute of Food Research, Norwich. NR4 7UA. UK

10 <sup>3</sup>School of Medicine, Keio University, Shinjuku-ku, Tokyo 160-8582 Japan

11 <sup>4</sup>Norwich Medical School, University of East Anglia, Norwich. NR4 7TJ. UK.

12

13

14 \*Corresponding author:

15 [carmen.pin@ifr.ac.uk](mailto:carmen.pin@ifr.ac.uk)

16 Tel: +441603255000

17 Fax: +441603507723

18

19

20

21



## 22 Abstract

23 Intestinal crypt fission is a homeostatic phenomenon, observable in healthy  
24 adult mucosa, but which also plays a pathological role as the main mode of growth of  
25 some intestinal polyps. Building on our previous individual based model for the small  
26 intestinal crypt and on *in vitro* cultured intestinal organoids, we here model crypt  
27 fission as a budding process based on fluid mechanics at the individual cell level and  
28 extrapolated predictions for growth of the intestinal epithelium.

29 Budding was always observed in regions of organoids with abundant Paneth  
30 cells. Our data support a model in which buds are biomechanically initiated by single  
31 stem cells surrounded by Paneth cells which exhibit greater resistance to viscoelastic  
32 deformation, a hypothesis supported by atomic force measurements of single cells.  
33 Time intervals between consecutive budding events, as simulated by the model and  
34 observed *in vitro*, were 2.84 and 2.62 days, respectively. Predicted cell dynamics was  
35 unaffected within the original crypt which retained its full capability of providing  
36 cells to the epithelium throughout fission. Mitotic pressure in simulated primary  
37 crypts forced upward migration of buds, which simultaneously grew into new  
38 protruding crypts at a rate equal to  $1.03 \text{ days}^{-1}$  in simulations and  $0.99 \text{ days}^{-1}$  in  
39 cultured organoids. Simulated crypts reached their final size in 4.6 days, and required  
40 6.2 days to migrate to the top of the primary crypt. The growth of the secondary crypt  
41 is independent of its migration along the original crypt. Assuming unrestricted crypt  
42 fission and multiple budding events, a maximal growth rate of the intestinal  
43 epithelium of  $0.10 \text{ days}^{-1}$  is predicted and thus approximately 22 days are required for  
44 a 10-fold increase of polyp size. These predictions are in agreement with the time  
45 reported to develop macroscopic adenomas in mice after loss of *Apc* in intestinal stem  
46 cells.

47  
48  
49

## 50 Introduction

51 The process of crypt fission, in which two functional crypts develop from one  
52 single crypt, is a rare phenomenon in the healthy small intestinal or colorectal mucosa  
53 of adults, but is essential for maintaining and recovering epithelial homeostasis  
54 following severe chemical-induced crypt injury <sup>1</sup>, cytotoxic chemotherapy <sup>2</sup>, or  
55 irradiation <sup>3</sup>. Crypt fission is also responsible for increasing the number of crypts  
56 required for postnatal development of the intestine <sup>4,5</sup>, and for the sustained expansion  
57 of the mucosal surface area following intestinal resection <sup>6</sup>. Thus, this phenomenon  
58 regulates mucosal morphology in the large intestine, and the balance between  
59 population size of crypts and villi in the small intestine <sup>7</sup>. It has also been reported that  
60 crypt fission is instrumental in the growth of epithelial tumours and in particular, in  
61 the growth of adenomatous polyps bearing mutations of the adenomatous polyposis  
62 coli (APC) gene <sup>8,9</sup>, colorectal adenomas and hyperplastic polyps <sup>10-12</sup> and in small  
63 bowel polyposis syndromes including familial adenomatous and hamartomatous  
64 syndromes such as juvenile polyposis<sup>13,14</sup>.

65 The mechanisms regulating the rate of crypt fission remain unclear. A crypt  
66 cycle has been postulated in which a small alteration in the balance between cell loss  
67 and cell proliferation results in a slow process of crypt enlargement and a gradual  
68 compression of cells located in the lower part of the crypt, which is relieved by the  
69 buckling of the cell layer out of the crypt base which initiates the fission event <sup>15</sup>.  
70 Stochastic models have been applied to explore the stability and asymptotic behaviour  
71 of the crypt cycle <sup>16</sup>. In the human colon, calculations indicate a crypt cycle time of  
72 between 17 and 30 years <sup>12</sup>, while in the mouse the length of the crypt cycle is 0.3-3.6  
73 years <sup>15,17</sup>. A simple model postulates that the threshold for triggering crypt fission is  
74 the doubling of the stem cell number <sup>18</sup>. Several biomechanical approaches, based on  
75 the behaviour of solids, have been developed to model buckling configurations in the  
76 intestinal epithelium as the result of the growth of the tissue and the elastic properties  
77 of the epithelium and/or underlying stroma <sup>19-23</sup>.

78 The main limitation to exploring crypt fission is its low frequency in the healthy  
79 mucosa combined with the difficulty of following the fission process in real time.  
80 Crypt fission is however frequently observed in cultures of intestinal organoids <sup>24-26</sup>.  
81 Crypts growing *in vitro* are rapidly sealed, forming a cyst containing a lumen filled  
82 with apoptotic cells. The surface of the cyst undergoes continuous budding events that

83 grow into crypts, which after protruding from the cyst, undergo fission. Paneth cells  
84 present at the base of the crypts and at budding sites<sup>25</sup> provide a crucial niche for  
85  $Lgr5^+$  stem cells by secreting Wingless/Int (Wnt) ligands<sup>27</sup>. Crypts deficient in Paneth  
86 cells require exogenous Wnt molecules in order to grow *ex vivo*, while factors  
87 compensating for the absence of Paneth cell-derived Wnt signals prevent stem cell  
88 exhaustion *in vivo*<sup>28</sup>. Buske et al<sup>23</sup> modelled the biomechanics of the formation of  
89 buds in the initial cyst, describing the surface of the continuously expanding cyst as an  
90 epithelial cell layer provided with a flexible basal membrane whose mechanical  
91 properties generate spontaneous proliferation-induced curvatures in the shape of the  
92 epithelium. These spontaneous curvatures lead to buckling configurations by inducing  
93 the specification into Paneth cells, which in a positive feedback fashion induce a more  
94 pronounced curvature of the epithelium, leading to the formation of the bud on the  
95 surface of the cyst<sup>23</sup>. The authors identified a set of conditions that lead to the  
96 formation of buds in a cyst in continuous expansion, but not for budding and fission in  
97 non-expanding crypts.

98       The purpose of our study was to advance our understanding of crypt fission by  
99 integrating biomechanical and cell-based computational models with measurements  
100 from fission events in *in vitro* cultured intestinal organoids. Based on empirical  
101 observations, we have extended the computational model previously developed for the  
102 crypt<sup>29</sup> by adopting an approach based on fluid mechanics that describes the  
103 displacement of cell material out of the crypt plane to form buds that grow into crypts.  
104 Our findings challenge the traditional belief that crypt fission is a process of crypt  
105 base enlargement followed by buckling, proposing instead that bud initiation is  
106 generated by the difference in the biomechanical behaviour of neighbouring Paneth  
107 and stem cells. The model hypothesizes that the new crypt develops without affecting  
108 cell dynamics within the original crypt. Under these conditions, the ability of the  
109 original crypt to supply cells to neighbouring villi is not altered throughout the fission  
110 process. Ultimately the model has been applied to predict maximal growth of the  
111 epithelium by unrestricted crypt fission.

## 112 **Results**

113

### 114 **Biomechanical modelling of bud formation**

115 In mouse intestinal organoid cultures, bud formation takes place initially in  
116 regions of the primary cyst with high Paneth cell density; initial buds grow into crypts  
117 which contain Paneth and stem cells intermingling at their bases (Figure 1). The new  
118 crypts undergo budding events that resemble the reported *in vivo* crypt fission  
119 phenomena. Figure 2 shows that in organoids crypt fission is a budding phenomenon  
120 that starts in regions of high Paneth cell density at the base of the crypts. The  
121 mechanism underlying the association of bud formation and Paneth cells is unknown.  
122 To circumvent this lack of knowledge, we have postulated that crypt fission is  
123 initiated as a budding process by stem cells surrounded by Paneth cells or their  
124 progenitors as a result of biomechanical forces.

125 The computational model previously developed for the crypt <sup>29</sup> describes the  
126 configuration of the crypt as a spiral in the crypt base and a helix forming a stack of  
127 circular rings. As described in the Methods section we have extended this approach by  
128 assuming that the crypt comprises viscoelastic epithelial cells adjacent to each other,  
129 and able to deform if a threshold force, which varies depending on the type of cell, is  
130 exceeded. Cell growth, division and migration affect the balance between the space  
131 required by cell material and the available space in the crypt wall, generating forces  
132 that act upon the cells. In response to these forces individual cells flow deforming the  
133 shape of the crypt wall and leading eventually to budding initiation. We assume that  
134 the proliferative condition of stem cells makes them deformable when subjected to  
135 forces generated by changes in their size during growth and division and/or in the  
136 available space in the crypt wall. For Paneth cells, deformation occurs when a critical  
137 force threshold is exceeded. In order to support this hypothesis, Atomic Force  
138 Microscopy (AFM) has been used to measure the Young's modulus of Lgr5-eGFP  
139 positive cells and Lgr5-eGFP negative large granular crypt cells. The Young's  
140 modulus is a measure of stiffness that quantifies the linear stress-strain relationship in  
141 the range of stress where Hook's law holds. Figure 3A shows that the Young's  
142 modulus of all but one of the Lgr5-eGFP positive cells was significantly smaller than  
143 that of large granular cells by more than 3 times the standard deviation. Lgr5-eGFP  
144 positive cells, which were assumed to be stem cells, required significantly smaller

145 forces to undergo deformation than large granular cells, which were assumed to be  
146 Paneth cells. Moreover, we have assumed that cells behave as viscous materials rather  
147 than the solid material behaviour described in previous models. Viscoelastic  
148 behaviour of cells was demonstrated in force curves. AFM measurements showed the  
149 typical separation, or hysteresis, between the approach and retract force curves  
150 resulting from viscous behaviour in all assessed cells (Figure 3B).

151 In order to parameterize our model, we have analysed the results in crypts  
152 simulated with several values for the shear stress threshold required for Paneth cells  
153 deformation.

154 Figure 4A compares the time intervals between successive budding events  
155 observed *in vitro* with those simulated using several values for the parameter  $\alpha$ . This  
156 parameter governs the force threshold required for Paneth cell deformation. When  
157  $\alpha=0$ , Paneth cells have identical mechanical properties to stem cells. When  $\alpha=1$ , the  
158 force required to deform Paneth cells is equal to the force generated by a  
159 disequilibrium between available and required space equal to one average cell size; if  
160  $\alpha$  is smaller or greater than 1, Paneth cell deformation requires forces smaller or  
161 greater, respectively, than that generated by one extra cell. When crypts were  
162 simulated with  $\alpha=0$  and  $\alpha=0.1$ , Paneth cells were deformed with changes in cell size  
163 translated in the flow of cell contents from crypt bottom to top without deformations  
164 of the crypt wall. This unimpeded flow was due to the non-stress boundary at the top  
165 of the crypt because of unrestrictive cell removal. As the value of  $\alpha$  increased, Paneth  
166 cells became more resistant to deformation so that the increase in size and/or decrease  
167 of available space during the cell cycle was not accommodated by the non-deformable  
168 neighbouring Paneth cells, leading to protrusion of cell material out of the crypt wall  
169 and bud formation. In simulated crypts, the frequency of budding increased rapidly as  
170 the value of  $\alpha$  increased from 0 to 1 (Figure 4B). The best agreement between  
171 simulated and observed distributions of frequencies for the time interval between  
172 successive budding events was observed for values of  $\alpha$  slightly greater than 1. For  
173 instance, the smallest difference between the simulated and observed distribution was  
174 detected for  $\alpha=1.3$  (Figure 4B). The median time interval between consecutive  
175 budding events observed *in vitro* and simulated with  $\alpha=1.3$  was 2.62 and 2.84 days,  
176 respectively. These medians were not significantly different ( $p > 0.05$ ). Moreover,  
177 under these assumptions bud formation was associated with single stem cells  
178 surrounded by Paneth cells. Figure 4C shows that the probability of budding of one

179 stem cell surrounded by Paneth cells increases as the resistance to deformation of  
180 Paneth cells increases, reaching values of 0.95 for  $\alpha > 1$ , while the probability of  
181 budding for stem cells clusters with 2, 3 or 4 stem cells is very low (ca 0.04) and  
182 practically not affected by the resistance of Paneth cells to deformation (Figure 4C).

183 In our original computational model <sup>29</sup>, the ratio of Paneth to stem cells is 3:2  
184 and they intermingle at the base of the crypt due to Notch signalling-driven  
185 differentiation. In the crypt base, stem cell descendants differentiate into Paneth cell  
186 progenitors or remain as pluripotent stem cells according to Notch signalling, which is  
187 activated and inhibits the secretory cell fate if more than 50% of cells in contact  
188 belong to the secretory lineage. In addition, cells in the crypt bottom are dynamically  
189 relocated to adjust for cell growth and division. These events determine the  
190 configuration of the crypt bottom. Figure 4D shows the relative frequency of stem  
191 cells clusters with 1 (0.18 relative frequency), 2 (0.32), 3 (0.28) or 4 (0.22) stem cells  
192 in simulated crypts, and how these frequencies were similar for all simulations and  
193 not affected by the resistance of Paneth cells to deformation or values of parameter  $\alpha$ .  
194 Figures 4 E-H show an upper view of the displacement of the cell centres on a ring of  
195 the crypt during cell deformation under selected mechanical scenarios. When all cells  
196 are stem cells (Figure 4E), or intermingling Paneth and stem cells are deformable with  
197 the same mechanical behaviour ( $\alpha=0$ , Figure 4F) deformations of the ring are not  
198 detected. When Paneth cells are more resistant to deformation than stem cells, for  
199 instance for  $\alpha=1.3$ , changes in the available space due to stem cells growth are not  
200 accommodated and lead to protrusion of cell material out of the crypt wall (Figures  
201 4G-H). We assume irreversible cell deformation if more than half of the cell material  
202 is protruding out of the plane of the crypt. Irreversible deformations are observed in  
203 areas where 1 stem cell is surrounded by Paneth cells alone (Figures 4G-H). In  
204 general, irreversible deformations were not detected when 2 or more stem cells are  
205 adjacent to each other because the threshold force for the viscoelastic behaviour of  
206 Paneth cells is reached before the irreversible protrusion of cell contents (Figure 4H).  
207 If the deformation is reversible, at division time, daughter cells locate out of the plane  
208 of the crypt. Those stem cell descendants located outside the crypt plane together with  
209 the surrounding Paneth cells, form an initial bud protruding from the original crypt  
210 that will grow into a new crypt. We have observed *in vitro* that Paneth cells from the  
211 original crypt appear to be incorporated into the new crypt (Figure 1) and it has been

212 demonstrated *in vivo* that crypts newly generated by fission contain numerous Paneth  
213 cells from the original crypts<sup>30</sup>.

214 We have assumed a fixed value for the limiting protruding cell material of  
215 irreversible deformations. Changing the protrusion threshold for budding would  
216 modify the probability of budding of stem cell clusters with different sizes. Should  
217 new experimental evidence in support of this mechanism be forthcoming, simulations  
218 could be run to fit jointly the parameters governing the force threshold for Paneth cell  
219 deformation and the protrusion threshold for bud initiation.

220

### 221 **Cell dynamics within crypts during fission**

222 Cell proliferation and differentiation takes place in the secondary crypt  
223 according to the hypotheses of the previously developed model<sup>29</sup>. We assumed that  
224 mitotic pressure in the primary crypt forces the upward migration of the secondary  
225 crypt, which simultaneously grows and protrudes out of the primary crypt. The  
226 supplementary Video S1 shows a simulation of a crypt fission event and Figure 5A  
227 shows good agreement between the specific growth rates of the new crypt observed  
228 experimentally (0.99 days<sup>-1</sup>) and in the simulations (1.03 days<sup>-1</sup>) (Figure 5A). The  
229 median values were not significantly different ( $p > 0.05$ ). The good agreement  
230 between the growth rates of the secondary crypt in simulated and in observed fission  
231 events indicates that the elongation of the secondary crypt is likely based on cell  
232 proliferation, which takes place at the same rate as in the primary crypt.

233 In simulated fission events the upward migration of the secondary crypt along  
234 the original crypt has two periods. The first has a very slow migration rate, with the  
235 new crypt located at the base of the original crypt, with a second period of rapid  
236 upward migration along the primary crypt (Figure 5B). The duration of the first period  
237 of very slow migration is highly variable and lasts until the new crypt reaches  
238 positions above row 5 in the original crypt, which requires  $4 \pm 3.3$  days. Thus, during  
239 the first period some new crypts may fully develop at the base of the original crypt  
240 without migrating upwards. This event, predicted by the model, is observed in  
241 cultured organoids such as that captured in Figure 6 showing a fully developed crypt  
242 at the base of the primary crypt and how this new crypt replaces the original crypt.

243 Once the secondary crypt reaches positions above the base of the original crypt,  
244 it rapidly migrates upwards to the top of the original crypt, which takes on average  $1.7$   
245  $\pm 0.72$  days. Our model therefore predicts that the bud is confined to the lower portion

246 of the crypt for approximately 70% of the duration of the fission process. In  
247 agreement with this prediction, between 70 to 90% of the observed fission events  
248 have been reported to be detected in the lower 1/4 of the crypts in infant rats <sup>7</sup>. In a  
249 study of acid injury, most fission events were observed in the lower 2/3 of the crypt <sup>1</sup>.

250 The predicted increase in migration velocity after reaching positions above the  
251 crypt base is in agreement with the observed dependency of the migration velocity  
252 along the crypt on mitotic pressure, which is greater at higher positions in the crypt <sup>31</sup>.  
253 Forces derived from cell growth and division in the primary crypt are sufficient to  
254 explain the upward migration of the secondary crypt along the primary crypt, as seen  
255 in the close agreement between simulated and observed migration rates (Figure 5A).  
256 The Supplementary Video S2 shows a simulation of a crypt undergoing fission and an  
257 *in vitro* fission event in an organoid during 1.3 days of the period of rapid migration  
258 of the secondary crypt.

259 In our model, growth and migration of the secondary crypt are independent of  
260 each other while cell proliferation and migration within the original crypt are not  
261 affected during fission. This has important implications for the functionality of the  
262 original crypt, which supplies cells to the *villi* at full capacity throughout the fission  
263 process. Figure 7 shows the analysis of the simulation results regarding growth and  
264 migration of the secondary crypt. The median time required for the new crypt to reach  
265 its final size was 4.6 days (Figure 7A) while the median time to reach the top of the  
266 primary crypt was 6.2 days (Figure 7B). These timings agree with the results of a  
267 morphological study of the epithelium regeneration after acid injury <sup>1</sup> in which crypt  
268 fission was observed 7 days after the injury and the normal appearance of the mucosa  
269 was recovered by 14 days post-injury.

270 Approximately 30% of the simulated crypts reached their final size before  
271 reaching positions above row 5 on the primary crypt (Figure 7C). From these crypts,  
272 the 5% located at row 0 of the original crypt have a small probability of migrating  
273 upwards and could eventually replace the original crypt as observed *in vitro* (Figure  
274 6). Some of the remaining 25% of crypts located at the bottom of the primary crypt  
275 could ascend along the original crypt, generating lateral branches and resembling the  
276 reported asymmetrical fission events commencing on the lateral crypt walls instead of  
277 at the crypt base<sup>8, 10</sup>. Only 3% of the new crypts reach the top of the primary crypt  
278 with a small size, equivalent to 10% of the final size of the crypt (Figure 7D). About



279 75% of the new crypts reach their final size before reaching the top of the primary  
280 crypt or the lumen (Figure 7D).

281

### 282 **Cell composition in crypts during fission**

283 During expansion of the new crypt, stem cell descendants generated at the crypt  
284 base under high Wnt signalling give rise to stem cells and Paneth-secretory cells,  
285 while the progeny of stem cells above the crypt base under low Wnt signalling will  
286 specify into proliferative absorptive progenitors and secretory-goblet, enteroendocrine  
287 and Tuft cells. Deciding between the two fates of secretory and stem/absorptive cells  
288 depends on Notch signalling. Our model hypothesis for the crypt is that Notch  
289 signalling inhibits secretory fate if more than 50% of the cells they are in contact with  
290 belong to the secretory lineage<sup>29</sup>. We have assumed that mature enterocytes are not  
291 generated in the new crypt during its expansion.

292 Figure 8 shows that the simulated average proportions for each cell type in the  
293 crypt remain fairly constant during fission. Around the third day after fission  
294 commences, the model predicts a slight increase in the proportion of Paneth and stem  
295 cells (Figure 8A). Acute activation of  $\beta$ -catenin has been reported to result in frequent  
296 budding events at the bottom of colonic crypts *in vivo* accompanied by an increase of  
297 the stem cell compartment<sup>32</sup>. Our model predicts that this increase is coincidental with  
298 the formation of the bud or stem cell niche for the new crypt but it is rapidly averaged  
299 out by the growth of the bud into a new crypt containing all cell types. Thus, the  
300 predicted size of the proliferative compartment during fission is on average unaffected  
301 (Figure 8B). The deletion of the adenomatous polyposis coli (*Apc*) gene in intestinal  
302 stem cells of mice leads to an aggressive expansion of adenomatous polyps by crypt  
303 fission. However the proportion of  $Lgr5^+$  stem cells in tumors remained unchanged  
304 with respect to healthy crypts<sup>9</sup>. Similarly, the number of mitotic cells and the size of  
305 the cell proliferation compartment in human familial adenomatous polyposis (FAP)  
306 crypts or in mouse multiple intestinal neoplasia (MIN) crypts did not differ from that  
307 of healthy crypts<sup>8</sup>.

308

### 309 **Predicting growth of the intestinal epithelium by unrestricted crypt fission**

310 The growth of the intestinal epithelium by crypt fission was predicted based  
311 upon the assumption that budding and fission always take place in crypts when a stem  
312 cell is surrounded by Paneth cells. Therefore, crypts undergo more than one budding

313 process simultaneously with budding taking place in the new crypts generated by  
314 fission. These assumptions are based on *in vivo* observation of multiple buds arising  
315 from the same crypt as reported after injury<sup>3</sup>.

316 Figure 9 shows that the predicted value for the specific growth rate of the  
317 intestinal epithelium by crypt fission is approximately  $0.10 \text{ days}^{-1}$ . Thus, about 15.3  
318 and 21.9 days are required to observe a 5 and 10-fold increase in size, respectively.  
319 The predicted growth of the epithelium by unrestricted crypt fission agrees with *in*  
320 *vivo* observations in mice after inducing the loss of the *Apc* gene in intestinal stem  
321 cells<sup>9</sup>. After *Apc* loss, crypt branches were continuously formed resulting in  
322 macroscopic epithelial formations 2-3 weeks post-induction<sup>9</sup>. However, the constant  
323 specific growth rate observed *in vitro* and estimated for adenoma formation in *Apc*<sup>-</sup>  
324 mice seems to differ from the growth kinetics reported for human colonic adenomas.  
325 These included relatively mitotically old populations of monoclonal crypts with  
326 occasional newly generated subclones, indicating that colorectal tumourigenesis may  
327 be characterized by relative stasis with occasional rapid growth of sub-clones<sup>33</sup>.

328 The predicted percentage of crypts undergoing fission in the epithelium was  
329 ~37.6% (Figure 9) comparable with prior *in vivo* studies reporting values of 35% and  
330 22% in mice<sup>34, 35</sup>, and 18% in humans at fission peaks seen during intestinal  
331 development in infants<sup>36</sup>. The percentage of crypt fission events observed in the  
332 proximal small bowel of MIN mice varied from 5% to 22%<sup>8</sup>.

333

## 334 Discussion

335 Our individual cell-based approach to modelling the initiation of budding in the  
336 intestinal crypt is based on fluid mechanics with cells having heterogeneous  
337 viscoelastic properties depending on their lineage. Our model challenges the  
338 traditional belief that crypt fission is a process of crypt base enlargement followed by  
339 buckling. We propose the formation of a bud that progressively grows into a crypt,  
340 migrating upwards along the primary crypt without affecting cell proliferation and  
341 migration within the primary crypt, and without compromising the primary crypt  
342 capability of providing cells to the epithelium.

343 Deformations are caused by the forced displacement of cell contents out of the  
344 crypt plane forming a bud containing the stem cell niche that will grow into a new  
345 crypt protruding from the primary crypt. Simulations under the hypothesis that Paneth

346 cells are more resistant to deformation than stem cells resulted in budding in regions  
347 of stem cells surrounded by Paneth cells, as observed in crypt organoid cultures. In  
348 our model, the location of buds depends on the local cell composition determined by  
349 Wnt- and Notch-driven cell differentiation, proliferation and migration within the  
350 crypt. Crypts with few Paneth cells are unlikely to undergo fission events, while an  
351 increase in the ratio of Paneth cells to stem cells increases the predicted frequency of  
352 budding. The model hypothesis could be generalized for the whole crypt by assuming  
353 that proliferative absorptive progenitors behave mechanically as stem cells while  
354 secretory cells have the same deformation threshold as Paneth cells. Budding takes  
355 place only when proliferative cells are surrounded exclusively by secretory cells. In  
356 normal conditions, this configuration would only be observed in the stem cell niche at  
357 the base of the crypt.

358         The mechanisms responsible for the initiation of buds in the intestinal crypt,  
359 both *in vivo* and *in vitro*, are as yet unknown. Although the hypothesis underlying  
360 bud initiation in our fluid mechanics approach lacks experimental evidence, the good  
361 agreement between the observed budding frequency *in vitro* and the frequency  
362 predicted by our biomechanical approach for the normal ratio between Paneth and  
363 stem cells in the crypt validates its use to predict epithelial growth by crypt fission.

364         Biomechanical approaches are commonly applied to modelling the buckling of a  
365 growing epithelium. The analysis of the patterns created by buckling of a dividing  
366 epithelial monolayer of cells lying on top of an elastic stroma results in a variety of  
367 possible conformations of crypts and villi along the small intestinal epithelium<sup>21, 37</sup>}.  
368 Modelling a growing epithelium attached to a basement membrane has also been  
369 demonstrated to be useful to study interactions between epithelium and stroma in the  
370 crypt<sup>38</sup>. This kind of biomechanical approach has been applied specifically to model  
371 crypt fission<sup>19, 20, 22, 39</sup>. These models consider the epithelium as a solid beam formed  
372 by adjacent cells subjected to stretching and compression forces generated by an  
373 increase in the number of cells, leading to buckled conformations. The cell-based  
374 approach of Drasdo<sup>19</sup> and Drasdo and Loeffler<sup>39</sup> describes the bending of the  
375 epithelium in a two dimensional system and identifies cell proliferation as the main  
376 reason for the onset of buckling. In the continuous approach modeling of Edwards and  
377 Chapman<sup>20</sup>, the epithelium is modeled as a growing beam attached to an underlying  
378 lamina in 2 dimensions. In this model, the buckling of the tissue is in response to any  
379 combination of an increase in cell proliferation, an enlargement of the proliferative

380 compartment and/or an increase in the strength of cellular attachment to the  
381 underlying lamina. A further analysis of this approach shows that non-uniform growth  
382 patterns along the epithelium have a much weaker influence on the buckled shapes  
383 than non-uniformities in the mechanical properties of the material <sup>22</sup>. The same  
384 authors have recently claimed that in a three-dimensional system, growth patterning  
385 has a greater impact on the distribution of crypts than does material inhomogeneity<sup>37</sup>.  
386 A distinctive feature of our approach to modelling crypt fission is that we treat cells as  
387 viscous materials rather than assuming the solid material behaviour described in the  
388 models discussed above. In agreement with *in vitro* experimental observations, we  
389 have modelled fission as a budding process based on fluid mechanics at the individual  
390 cell level and not, as the folding or buckling of solid material. AFM measurements  
391 confirmed the viscous nature of both LGR5-eGFP positive and LGR5-eGFP negative  
392 large and granular single cells isolated from crypts (Figure 3B). Moreover, we  
393 modelled fission as a consequence of inequalities in the mechanical properties of  
394 viscoelastic cells which depend on cell lineage. This hypothesis was also supported  
395 experimentally by AFM measurements of single cells, which revealed that stem cells  
396 are less stiff than other granular large crypt cells.

397 Another distinctive feature of our model is that, changes in the size of the  
398 proliferative compartment or in the division rate are not associated with budding.  
399 Although fission ultimately depends on cell division, there is uncertainty regarding  
400 the relationship between changes in cell proliferation and crypt fission. The increase  
401 in cell proliferation within the crypt, or in crypt volume, has been reported in several  
402 studies not to be associated with crypt fission<sup>10, 40-42</sup>. Indeed, the administration of  
403 epithelial growth factor to MIN mice resulted in an increased cell proliferation within  
404 crypts with a significant reduction in the rate of fission <sup>41</sup>. Similarly, studies on  
405 intestinal development in infant rats and humans concluded that crypt fission is not  
406 always preceded by crypt hyperplasia<sup>36, 42</sup>. Also, the administration of P-cadherin  
407 results in enhancement of crypt fission *in vivo* while cell proliferation in crypts is  
408 unaffected <sup>43</sup>. Similarly, in MIN mice the proportion of crypts in fission increases  
409 dramatically but cell proliferation is not affected in dividing crypts compared to stable  
410 crypts <sup>8</sup>. In another study, a reduction in intestinal crypt fission was detected after the  
411 administration of the negative regulator of Wnt signalling, dickkopf, although cell  
412 proliferation remained unchanged <sup>44</sup>.

413 *Apc* loss induces acute activation of Wnt/ $\beta$ -catenin signalling pathway. The  
414 activation of the Wnt pathway induces *de novo* specification of Paneth cells in the  
415 mouse small intestine. Both murine colon polyps and human colonic tumours  
416 resulting from *Apc* mutations express genes involved in Paneth cell differentiation<sup>45</sup>.  
417 Although Paneth cells are absent from both mouse and human colon, a subset of  
418 colonic secretory cells that share cKit<sup>+</sup> expression with small intestinal Paneth cells,  
419 and are essential for the maintenance of the stem cell niche and for organoid  
420 formation *in vitro*, have been identified in the base of colonic crypts intermingled with  
421 Lgr5<sup>+</sup> cells<sup>46</sup>.

422 In the small intestine, the relationship between Paneth cells and the two pools of  
423 intestinal stem cells, slow cycling cells located at position +4 and actively cycling  
424 stem cells at the bottom of crypt, is not well understood. It has been demonstrated that  
425 Paneth progenitor cells revert to stem cells upon crypt damage<sup>47, 48</sup>, and specifically  
426 quiescent +4 stem cells have been identified with secretory progenitors expressing  
427 Lgr5 and able to regain 'stemness' after intestinal injury<sup>49, 50</sup>. In mouse colonic crypts  
428 Wnt activation has been demonstrated to induce crypt fission, accompanied by a  
429 reduction in the cell proliferation rate and of activation of the Notch signalling  
430 pathway among progenitors<sup>32</sup>. Therefore under Wnt activation, crypt fission could be  
431 associated with enhancement of the slowly cycling secretory progenitors, which is in  
432 agreement with the increase of budding linked to the increase in the ratio of secretory  
433 cells to stem cells predicted by our model.

434 We have observed buds in regions with Paneth cells although we have not  
435 experimentally determined the density of Paneth cells in budding regions. It has been  
436 reported that numerous Paneth cells from the primary crypt are detected in newly  
437 generated crypts by fission *in vivo*<sup>30</sup>. In this published study, crypt fission is assumed,  
438 though not experimentally proven, to be a progressive longitudinal partition initiated  
439 at the crypt base. However, if fission is a budding process as we propose here, the  
440 abundance of original Paneth cells in the base of the new crypt indicates that Paneth  
441 cells or their progenitors are present in high numbers in the region where the bud is  
442 initiated and they form part of the initial bud. On the other hand, an essential role of  
443 Lgr5<sup>+</sup> stem cells in crypt fission in the intestine<sup>30</sup> and also in gland fission in the  
444 stomach<sup>51</sup> has been demonstrated using *in vivo* clonal fate mapping strategies to  
445 observe the lateral expansion of Lgr5-expressing stem cell derived clones, containing  
446 clonal Lgr5<sup>+</sup> stem cells.

447 It should be noted however that ablation of Paneth cells does not affect  
448 deregulation of crypt fission and intestinal tumourgenesis in *Apc* mice with intestinal  
449 stem cells deficiency<sup>28</sup>. Non-canonical Wnt signalling has also been associated with  
450 crypt regeneration in the wounded epithelium of mice<sup>52</sup>. Wnt5a molecules, which are  
451 non-canonical Wnt ligands that inhibit intestinal cell proliferation *in vitro*, have been  
452 detected in stromal mucosal cells localized to clefts in-between nascent crypts *in vivo*,  
453 seemingly contributing to defining the shape of the new crypts in injured areas of the  
454 epithelium where crypts have been excised<sup>52</sup>. A common denominator seen in  
455 circumstances preceding non-tumour growth-associated crypt fission *in vivo* is a  
456 diminished density of functional healthy crypts in the mucosa. For example, as seen  
457 during intestinal growth in infants<sup>35, 36</sup>, compensatory intestinal dilation following  
458 intestinal resection<sup>6</sup>, and during recovery of wounded areas of the mucosa<sup>1, 52</sup>. The  
459 role of Wnt signalling and Paneth cells in the regulation of crypt fission *in vivo* is  
460 therefore complex and other components, potentially of mesenchymal origin, are  
461 likely to be involved.

462 In our simulated crypts, unrestricted crypt fission is associated with a  
463 biomechanical instability generated by difference in the biomechanical properties of  
464 Paneth and stem cells. We can hypothesize that the progression of the instability to  
465 form an initial bud is inhibited *in vivo*, while the inhibitory mechanism is absent in the  
466 *in vitro* culturing system. This hypothesis was developed to circumvent the lack of  
467 information regarding the signalling and regulation of the fission process. Although  
468 under this hypothesis the predicted and observed budding frequencies are in good  
469 agreement (Figure 4A), further experimental validation is required. In addition, the  
470 cellular Wnt and Notch signalling pathways function normally in both the simulated  
471 crypts and in the *in vitro* cultured crypts. However, *Apc*<sup>-/-</sup> mice have a severely altered  
472 Wnt signalling pathway. Therefore, although the rates of fission appear to be similar,  
473 the mechanisms behind unrestricted crypt fission *in vivo* and *in vitro* are likely to be  
474 very different. One of the essential factors required to maintain intestinal stem cells  
475 and organoids in culture is R-spondin<sup>53</sup>. This protein strongly potentiates the Wnt  
476 signalling pathway and, just as in the case of the deletion of the Wnt signalling  
477 inhibitor APC *in vivo*<sup>8, 12, 54</sup>, this may account for the unimpeded epithelial growth by  
478 crypt fission observed *in vitro*. Thus, crypts cultured *in vitro* under acute stimulation  
479 of the Wnt signalling pathway, and *in vivo* crypts with a disinhibited Wnt target gene

480 programme, may achieve maximum crypt fission rates, which would explain the  
481 similarity of the epithelium growth kinetics in these two different systems.

482 In summary, the model we have presented shows how crypt budding can be  
483 biomechanically initiated by stem cells surrounded by Paneth cells which accurately  
484 predicts epithelial growth by unrestricted crypt fission as observed in cultured  
485 organoids. The epithelial growth rate predicted by unrestricted crypt fission agrees  
486 with the growth observed *in vivo* in intestinal adenomas associated with APC loss. We  
487 have therefore integrated individual based models with *in vitro* culturing organoids to  
488 develop an approach able to simulate the process of crypt fission and further  
489 extrapolated predictions for the growth of adenomatous polyps in the mouse intestinal  
490 epithelium. The generated modelling framework can be applied to test hypotheses on  
491 regulation mechanisms in homeostatic crypts and to explore the impact of  
492 perturbations on the progression of adenoma-carcinoma processes in the intestine.

**493 Methods**

494 Animal care and experimentation were performed in accordance with the Guidelines  
495 established by the Committee on Animal Care and Use of Keio University and under  
496 the authority of the UK Home Office (PPL 80/2355).

**497 Preparation of *in vitro* crypt cultures**

498 Small intestinal crypt preparations from 6 week old mice (strain C57/B6 or  
499 Lgr5-EGFP-ires-CreERT2) were embedded in Matrigel (BDBioscience). After  
500 polymerization of Matrigel, crypt culture medium (advanced DMEM/F12  
501 supplemented with Penicillin/Streptomycin, 10 mM HEPES, Glutamax, 1x N2, 1x  
502 B27 [Invitrogen], and 1  $\mu$ M N-acetylcysteine [Sigma] and containing 50 ng/ml EGF  
503 [Peprotech], 100 ng/ml noggin [Peprotech], 1  $\mu$ g/ml R-spondin 1) was overlaid.  
504 Cultures were maintained as previously described<sup>53</sup>.

505 The growth of organoids was imaged using a climate-controlled (37°C, 5%  
506 CO<sub>2</sub>) stage of an inverted motorised time-lapse microscopic system (Nikon) for  
507 periods of up to 10 days. Frames of ten movies including 1-3 organoids each were  
508 analysed to estimate budding frequency per crypt, the growth of the secondary crypt  
509 and its migration along the original crypt.

510

**511 Fluorescent immunostaining and confocal microscopy**

512 Organoids were isolated from Matrigel using Cell Recovery solution (BD  
513 Biosciences) and fixed with 4% paraformaldehyde (PFA). After fixation, samples  
514 were incubated with 0.2% Triton X-100 in PBS for permeabilization, and with  
515 Universal Blocking Reagent (Biogenex) for blocking non-specific binding of  
516 antibodies. To visualize Lgr5+ stem cells and lysozyme+ Paneth cells, samples were  
517 incubated overnight at 4°C with antibodies specific for GFP (abcam; ab6673, 1:100)  
518 and Lysozyme (Dako; A0099, 1:1000) in PBS. GFP and Lysozyme were labelled by  
519 anti-Goat alexa488 conjugated antibody and anti-Rabbit alexa568 conjugated  
520 antibody (Invitrogen) in PBS. Nucleus was counterstained with Hoechst33342.  
521 Images were acquired by confocal microscopy (Leica SP8).

522

**523 Crypt and epithelial cell isolation**

524 Crypts were isolated from whole small intestine of C57BL/6-J or Lgr5-  
525 eGFP<sup>tm1(cre/ERT2)Cle/J</sup> adult mice at 12-16 weeks of age. Whole intestines were flushed,



526 and dissected in PBS containing antibiotics and antimycotics. Samples were  
527 incubated on ice in 2 x 5 mins 1mM DTT and 3 x 5 mins 2mM EDTA, with gentle  
528 shaking to remove debris and sloughed epithelial cells. Remaining epithelial cells and  
529 crypts were dislodged by 30 min incubation in 2mM EDTA at room temperature, then  
530 vigorously shaken in successive fractions of ice-cold PBS. Crypts were spun down,  
531 concentrated and incubated 35 min at 37°C with collagenase/dispase (Roche) and  
532 DNase I (NEB) to generate a single-cell suspension. GFP-positive (Lgr5-eGFP stem  
533 cells) and GFP-negative cells (non-stem epithelial cells) were separated using a Sony  
534 SH-800 cell sorter. Cells were re-suspended in advanced DMEM containing B27, N2,  
535 n-acetylcysteine (1 mM), HEPES (10 mM) penicillin/streptomycin (100 U/ml), L-  
536 Glutamine (2 mM), epidermal growth factor (50 ng/ml), Wnt-3A (100 ng/ml), Noggin  
537 (100 ng/ml) SB202190 (20  $\mu$ M), seeded onto poly-lysine coated slides and allowed to  
538 adhere overnight at 37°C / 5% CO<sub>2</sub>. Media was replaced with D-PBS with  
539 Ca<sup>2+</sup>/Mg<sup>2+</sup>, immediately prior to measurement by atomic force microscopy.

540

#### 541 **Atomic Force Microscopy AFM**

542 The AFM used for this study was an MFP-3D-BIO (Asylum Research, Santa Barbara,  
543 CA. USA). The deformability measurements were performed with a cantilever fitted  
544 with 2.5  $\mu$ m diameter silica bead in place of the AFM tip (CP-PNPL-SIO-A, sQUBE  
545 Surface Science Support, Germany). This is necessary for two reasons; firstly to  
546 prevent penetration of the cell membrane by the AFM tip during the measurements,  
547 and secondly to allow proper quantification of the indenter shape for subsequent  
548 modelling<sup>55</sup>.

549 Prior to the cell deformation measurements, the optical lever sensitivity of the  
550 cantilevers was calibrated by pressing against a rigid surface (clean glass slide) The  
551 spring constants of the cantilevers were determined using the thermal noise spectra  
552 method<sup>56</sup>. The AFM sits on top of an inverted optical microscope (IX-71, Olympus,  
553 Japan) enabling the AFM tip to be accurately positioned on chosen cells. The optical  
554 microscope was operated in epi-fluorescence mode to enable discrimination of the  
555 Lgr5-eGFP+ stem cells. Deformability of the cells was measured by performing  
556 multiple force versus distance curves at a velocity of 2  $\mu$ m.s<sup>-1</sup> on the chosen cells.  
557 Two controlled maximum load forces (600 pN and 1.2 nN) were applied to ensure  
558 sufficient, but not excessive, deformation was achieved. The data was fitted to a

559 Hertzian elastic model featured in the instrument software which analyses it in terms  
560 of force versus indentation (MFP-3D 111111+1610).

561

### 562 **Biomechanical model for the initiation of buds**

563 Cells are modelled as spherical shapes of incompressible homogenous viscous  
564 material which are packed to form the walls of the crypt. Cells maintain their shape in  
565 the absence of stress, but under an applied sufficient stress, cell material flows and  
566 changes cell shape, accumulating stress in return. When the accumulated stress and  
567 the applied stress have the same magnitude, the cell material is no longer displaced.  
568 When the applied stress is removed, cells could partially return to their original form  
569 (viscoelastic behaviour) or maintain some degree of deformation (viscoplastic  
570 behaviour); constant cell proliferation generates a certain compression force in the  
571 system that prevents the absolute relaxation of the system.

572 We describe the crypt as a cylindrical structure organized in 3 dimensions with  
573 rings of cells in the XY horizontal plane and a vertical axis, Z, from the base to the  
574 top of the crypt (Figure 10). Proliferative cells, which include stem cells, are assumed  
575 to behave as Newtonian fluids under forces derived from cell growth; however mature  
576 cells including Paneth cells, behave as Bingham plastics. With these assumptions, the  
577 viscoelastic behaviour of stem cells is defined by one parameter, the dynamic  
578 viscosity coefficient,  $\mu$ , derived from the linear relationship between the shear force,  
579  $\tau$ , and the shear rate,  $\partial v/\partial x$ . For laminar flows this can be expressed as:  $\tau = \mu(\partial v/\partial x)$   
580 where  $v$  is the velocity and  $x$  the orthogonal dimension to the direction of the flow.  
581 The behaviour of Paneth cells is described by two parameters, the apparent viscosity  
582 coefficient,  $\eta$ , and the shear stress threshold or yield point,  $\tau_T$ , i.e.  $\tau = \tau_T + \eta(\partial v/\partial x)$ .  
583 Paneth cells exhibit linear shear stress, shear rate behaviour only after the shear stress  
584 threshold,  $\tau_T$ , has been reached. Hence, to deform Paneth cells, the driving shear stress  
585 has to be larger than  $\tau_T$ , and because of this threshold, Paneth cell deformation differs  
586 from stem cell deformation. The shear rate or velocity gradient,  $\partial v/\partial x$ , of Newtonian  
587 fluids decreases gradually towards the cell centre and reaches a value of 0 at the axis  
588 of symmetry or  $x = 0$  giving place to a gradual deformation of the shape of the edge  
589 (Figure 10). Bingham plastics behave as solids when the force is below the shear  
590 stress threshold which results in the formation of a solid plug at the front of the

591 deformed edge of the cell moving with the flow (Figure 10), i.e.  $\partial v/\partial x=0$  at  $x = x_T$ ,  
 592 which is the radio of the solid plug.

593 Assuming zero-stress boundary conditions at the top of the crypt because of the  
 594 unrestrictive removal of cells, when all cells have the same mechanical properties, cell  
 595 growth is translated in the flow of cells in the parallel direction to the Z axis within  
 596 the crypt wall. Flow within the crypt wall in other directions is also possible, but not  
 597 frequent, due to the fully packed condition of the crypt walls. The other direction that  
 598 the flow may take is the orthogonal direction to the Z axis, out of the crypt wall  
 599 (Figure 10).

600 When Paneth cells behave as Bingham plastics, the flow may be disturbed by  
 601 the presence of these cells with higher resistance to deformation which are obstacles  
 602 to the flow of the viscous cells, and eventually they may force the change of the  
 603 direction of the flow towards the X and Y directions, i.e. deforming the external side  
 604 of the crypt wall (Figure 10).

605 The deformation of the external side of the cells occurs when one or more  
 606 adjacent viscous, i.e. deformable, cells, whose geometric centres form a convex set,  
 607 are delimited by cells that will exhibit viscous behaviour only after a given threshold  
 608 force is reached. Flow analysis in three dimensions can be carried out under the  
 609 assumption of laminar flow. To analyse the deformation of the external side of the  
 610 cell, it is sufficient to analyse the flow in two dimensions in either the XZ plane or of  
 611 the XY plane as described in Figure 10. The analysis of the deformation in these two  
 612 planes is equivalent under the hypothesis of axial symmetric flow (Figure 10). As an  
 613 example, we describe below the deformation of rings formed by two- dimensional  
 614 cells in the XY plane (Figure 10). The analysis is exactly the same for a two-  
 615 dimensional longitudinal section of the crypt.

616 The Navier-Stokes general equations for an incompressible two-dimensional  
 617 flow are:

$$618 \quad \frac{\partial v_y}{\partial t} + v_x \frac{\partial v_y}{\partial x} + v_y \frac{\partial v_y}{\partial y} = -\frac{1}{\rho} \frac{\partial P}{\partial y} + \nu \left( \frac{\partial^2 v_y}{\partial x^2} + \frac{\partial^2 v_y}{\partial y^2} \right) \quad (1)$$

$$619 \quad \frac{\partial v_x}{\partial t} + v_x \frac{\partial v_x}{\partial x} + v_y \frac{\partial v_x}{\partial y} = -\frac{1}{\rho} \frac{\partial P}{\partial x} + \nu \left( \frac{\partial^2 v_x}{\partial x^2} + \frac{\partial^2 v_x}{\partial y^2} \right) \quad (2)$$

620 And the continuity condition for incompressible flow,

$$621 \quad \frac{\partial v_x}{\partial x} + \frac{\partial v_y}{\partial y} = 0 \quad (3)$$

622 In equations (1) through (3),  $v_x$  and  $v_y$  are the velocity components of the flow in the  $x$   
 623 and  $y$  direction, respectively,  $t$  is time,  $\rho$  is density,  $\nu$  is the kinematic viscosity and  $P$   
 624 is the pressure per unit length, which is uniformly applied to the edges of a two  
 625 dimensional cell in the direction of the motion of the liquid due to compression  
 626 (Figure 10). Cell compression is derived from the difference between cell size and  
 627 available space. We have described the deformation of free external cell sides only.  
 628 The deformation of free internal cell sides facing the crypt lumen could be similarly  
 629 analysed. With a perfect laminar flow, the pressure in both internal and external cell  
 630 sides and therefore cell content displacement in each direction will be proportional to  
 631 the area of each cell side. Due to the organization of cells in rings the area of the  
 632 internal cell side is smaller than the area of the external side. For instance, in our  
 633 crypt, cell protrusion towards the lumen will be in average only 20% of the external  
 634 cell protrusion. In addition, it is likely that cell structural properties perturb the flow  
 635 and decrease cell displacement towards the lumen. For these reasons, we have  
 636 disregarded the analysis of cell protrusion towards the lumen of the crypt.

637 As described in Figure 10, the laminar flow in two dimensions driven by a  
 638 constant pressure gradient,  $-\partial P / \partial y = K$ , takes place essentially in the  $y$  direction and  
 639 hence,  $v_x = 0$  which when replaced into equation (3), produces  $\partial v_y / \partial y = 0$ . These  
 640 two conditions,  $v_x = 0$  and  $\partial v_y / \partial y = 0$ , simplify equations (1) and (2) to the following:

$$641 \quad \frac{\partial v_y}{\partial t} = -\frac{1}{\rho} \frac{\partial P}{\partial y} + \nu \frac{\partial^2 v_y}{\partial x^2} \quad (4)$$

$$642 \quad 0 = -\frac{1}{\rho} \frac{\partial P}{\partial x} \quad (5)$$

643 Equation (5) indicates that  $P$  is not a function of  $x$ , then  $\partial P / \partial y = dP / dy = -K$   
 644 which combined with in equation 4 results in the governing equation:

$$645 \quad \frac{\partial v_y}{\partial t} = \frac{K}{\rho} + \nu \frac{\partial^2 v_y}{\partial x^2} \quad (6)$$

646 Assuming that the flow is in steady state, i.e.  $\partial v_y / \partial t = 0$ , equation (6) becomes:

$$647 \quad \frac{d^2 v_y}{dx^2} = -\frac{K}{\mu} \quad (7)$$

648 For stem cells behaving as a Newtonian fluid,  $\mu = \rho\nu$  is the dynamic viscosity of  
 649 the fluid. The  $x$  variable describes the distance of the cell content being displaced from  
 650 the cell centre in the XY plane and hence takes values in the interval  $(-R, R)$  (Figure  
 651 10). With the condition,  $dv_y/dx = 0$  at  $x = 0$  derived from the axial symmetry  
 652 assumption, and the no-slip condition at the boundaries, i.e.  $v = 0$  at  $x = R$ , equation 7  
 653 has solution:

$$654 \quad v_y(x) = \frac{dy}{dt} = -\frac{K}{2\mu}(x^2 - R^2) \quad (8)$$

655 Equation 8 is the Poiseuille law for a two-dimensional fluid and it describes the  
 656 velocity of cell material located at a distance  $x$  from the cell centre in the XY plane

657 The area of the surface,  $S$ , displaced in  $dt$ , or flow rate, can be estimated by  
 658 integrating equation 8 on  $x$  from  $-0$  to  $R$  and multiplying the result by 2:

$$659 \quad \frac{dS}{dt} = \frac{2}{3} aR^3 \quad (9)$$

$$660 \quad \text{Where } a = \frac{K}{\mu}$$

661 For Paneth cells behaving as Bingham plastics,  $\eta = \rho\nu$  is the apparent viscosity  
 662 of the fluid and equation 6 is as follows

$$663 \quad \frac{d^2v_y}{dx^2} = -\frac{K}{\eta} \quad (10)$$

664 With the condition,  $dv_y/dx = 0$  at  $x = X_T$ , which is the radius of the symmetric  
 665 solid plug at the center of the flow (Figure 10) and the no-slip condition at the  
 666 boundaries, i.e.  $v = 0$  at  $x = R$  and at  $x = -R$ , equation 7 has solution:

$$667 \quad v_y(x) = \frac{dy}{dt} = -\frac{K}{\eta} \frac{(x^2 - R^2)}{2} + \frac{K}{\eta} X_T(x - R) \quad (11)$$

668 The corresponding flow rate is:

$$669 \quad \frac{dS}{dt} = 2 \left( \int_{X_T}^R -\frac{K}{2\eta}(x^2 - R^2) + \frac{K}{\eta} X_T(x - R) dx + X_T v_y(X_T) \right) =$$

$$670 \quad = b \left( \frac{2}{3} R^3 + \frac{1}{3} X_T^3 - R^2 X_T \right) \quad (12)$$

$$671 \quad \text{Where } b = \frac{K}{\eta}$$

672 As the cell material is incompressible, the value  $dS/dt$ , can be estimated from  
 673 the change in cell size and available space as follows:

$$674 \quad \frac{d\hat{S}}{dt} = \sum_{k \in I} \frac{dA(\text{cell}_k)}{dt} - \frac{dA(\text{space available for } I \text{ set})}{dt} \quad (13)$$

675 where  $I$  is the set of adjacent cells forming a convex set with identical viscous  
676 behaviour and  $A$  the area of surface.

677 Equation 9 and 12 are identical when the shear stress threshold in Paneth cells is  
678 equal to zero and Paneth and stem cells have the same coefficient of viscosity,  $\mu = \eta$ .  
679 Under these conditions, the values of the parameters  $a$  and  $b$ , can be estimated from  
680 equation 9 or 12 and 13, respectively. The assumption of equal coefficient of viscosity  
681 for stem and Paneth cells also simplifies the description of the shear stress threshold  
682 in Paneth cells as described below.

683 In order to quantify the formation of buds with different values for the shear  
684 stress threshold in Paneth cells,  $\tau_T$ , and to provide a rough biological interpretation,  
685 the relationship between the shear stress and the pressure gradient due to cell growth  
686 can be described as

$$687 \quad \tau(x) = -x \frac{dP}{dy} \quad (14)$$

688 And the shear stress threshold in Paneth cells can be expressed as:

$$689 \quad \tau_T = X_T K \quad (15)$$

690 By substituting in equation 11:

$$691 \quad v_y(x) = \frac{dy}{dt} = -\frac{K}{2\eta}(x^2 - R^2) + \frac{\tau_T}{\eta}(x - R) \quad (16)$$

692 From equation 9 for the flow rate in stem cells, an average pressure gradient can  
693 be estimated as a function of the average growth rate of the surface area of stem cells,  
694  $r_{av}$ , and an average stem cell ratio at birth,  $R_{av}$ , as follows:

$$695 \quad K_{av} = \frac{3}{2} \frac{\mu}{R_{av}^3} r_{av} \quad (17)$$

696 From equation 14 and 17, the average force exerted by the compression due to  
697 one extra cell can be described as follows;

$$698 \quad \tau_{av} = R_{av} K_{av} = \frac{3}{2} \frac{\eta}{R_{av}^2} r_{av} \quad (18)$$

699 From equation 18 and under the assumption that  $\eta = \mu$ , values for the ratio  $\tau_T /$   
700  $\eta$  in equation (16) can be chosen to be proportional to the average shear rate in stem  
701 cells

$$\frac{\hat{\tau}_T}{\eta} = \alpha \frac{\tau_{av}}{\mu} = \frac{3}{2} \frac{r_{av}}{R_{av}^2}$$

703 And therefore,

$$\hat{\tau}_T = \alpha \tau_{av} \quad (19)$$

705 Where  $\alpha$  is a factor of proportionality between the shear force threshold required  
 706 to deform Paneth cells and the compressive forces generated by a disequilibrium  
 707 between the required and the available space equal to one cell size;  $\alpha$  takes values  
 708 equal to or greater than zero. If  $\alpha=0$ , Paneth cells behave as a Newtonian fluid and its  
 709 deformability is identical to that of stem cells. If  $\alpha=1$ , the shear force threshold  
 710 required to deform Paneth cells is equal to the compressive forces generated by one  
 711 extra cell; if  $\alpha$  is smaller or greater than 1, Paneth cells deformation requires forces  
 712 smaller or greater, respectively, than those generated by one extra cell. The initiation  
 713 of budding and fission takes place because of the instability of the cell shape. We  
 714 assume irreversible cell deformation, if more than half of the cell material is  
 715 protruding out of the plane of the crypt. Less extreme deformations of the cell are  
 716 considered reversible. Thus, when the protrusion of cell material is significant, at  
 717 division time, daughter cells will locate out of the plane of the crypt, initiating a bud  
 718 that grows into a new crypt.

719 In order to study how budding depends on the shear force threshold of Paneth  
 720 cells, the probability of budding within a period of 12 and the time intervals between  
 721 successive budding events in a single crypt were quantified in simulations run with  $\alpha$   
 722 values equal to 0.1, 0.3, 0.5, 0.7, 0.8, 0.9, 1, 1.1, 1.2, 1.3, 1.5, 2.

723

#### 724 **Integration of the bud initiation process in the individual based model for the** 725 **crypt of Pin et al<sup>29</sup> and analysis of forces.**

726 The model of Pin et al<sup>29</sup> has been adapted to describe crypt fission in a three  
 727 dimensional crypt. Model parameters are summarized in Supplementary Table S1. In  
 728 the original model, the structure of the bottom of the crypt is modelled as a three-  
 729 dimensional spiral followed by the crypt body, which is a three-dimensional helix,  
 730 constructed from single cells organized in a one-dimensional chain. The position of  
 731 any cell in the spiral or helix is determined by the coordinates of the cells organized in  
 732 rings in the XY plane and the vertical coordinate Z, which describes the height  
 733 reached by cells in columns perpendicular to the XY plane. At each interval time of

734 the simulation, the three dimensional spiral and helix are re-built according to the  
735 change in cell, and division or deletion events. Growing cells expand homogenously  
736 in all directions. The increase in cell size in the vertical direction creates a force  
737 translated mostly in upward migration. Cell size changes in the horizontal plane are  
738 accommodated by changing the perimeter of the ring in the XY plane perpendicular to  
739 the crypt-villus axis.

740 In the new version of the model, growing cells expand in the vertical Z  
741 direction, unless the force generated by growth is not enough to deform neighbouring  
742 Paneth cells, which in that case are obstacles to the flow that force cell shape  
743 deformation in the XY plane protruding out of the crypt wall.

744 The Monte Carlo simulation previously described <sup>29</sup> has been extended by  
745 updating the cell viscous behaviour and accordingly cell position at each time-step.  
746 Time-steps include division times. All other cell properties such as size, type, age are  
747 updated as previously described <sup>29</sup>. A summary of the extended approach is as  
748 follows:

749 1) Proliferative and stem cells grow, increasing their size to reach twice their  
750 original size by division time according to the proliferation rates previously described  
751 <sup>29</sup>. Non-proliferative cells also grow at those rates until they reach their final size.

752 2) The viscous behaviour of non-growing cells, such as mature Paneth cells, and  
753 the sets of deformable cells are evaluated by comparing the ratio between the overall  
754 size of neighbouring deformable cells and the available space. Paneth cells subjected  
755 to forces that are not greater than the threshold and are not deformable and remain in  
756 their original position. The deformation out of the crypt plane of growing stem cells  
757 surrounded by non-deformable Paneth cells is quantified as described in the section  
758 above. When the protrusion of cell material is significant, at division time, the  
759 daughter cells will form a bud located out of the plane of the crypt.

760 3) In regions where all cells are deformable, the increase of cell size takes place  
761 within the crypt wall and the cell deforms mainly in the direction of the crypt  
762 longitudinal, or Z, axis. At each time step, the crypt is reorganized to accommodate  
763 changes in cell size, which are translated in changes in the Z coordinate for the  
764 majority of cells, while cell coordinates in the XY plane practically do not change.  
765 Dividing cells partition into two daughter cells with similar size which is randomly  
766 apportioned <sup>29</sup>. The division event does not imply any increase of cell size, however,  
767 in practice, after division the one dimensional chain used to build the three



768 dimensional helix has to be reorganized to assign an index to the new cell as  
769 previously described<sup>29</sup>. One of the daughter cells is assigned with the index of the cell  
770 located in the ring immediately above. The vertical adjustment of indices spreads  
771 upwards along the crypt until the cell in the last ring. The position and shape of the  
772 relocated cell are accommodated to fit the space occupied by the cell immediately  
773 above and this has an impact on cell displacement. To quantify this impact, we have  
774 measured the velocity of cells during time intervals that include index rearrangement  
775 and compared it with velocities of cells that do not change the ring. Supplementary  
776 Figure S1 shows the comparison of the total distance and the distance in each  
777 dimension travelled by cells during time intervals with and without index  
778 reassignment. We have estimated that on average index reassignment takes place in  
779 the crypt in 20% of the cell movements and it generally causes a small increase of the  
780 total travelled distance by the cell by affecting mainly cell displacement on the XY  
781 plane (Supplementary Figure S1); this is because cells are not aligned along the crypt  
782 wall. Despite the impact of the index reassignment process on cell displacement, our  
783 approach is a good approximation to describe continuous cell growth and migration  
784 and cellular compaction within the crypt in a similar way to lattice free models<sup>57-60</sup>  
785 and therefore, it differs from automata cell models using rigid lattices<sup>61, 62</sup> in which  
786 cells migrate by discontinuous large movements.

787 In our approach, cell migration is exactly modelled as the result of the balance  
788 of forces during the process of cell deformation out of the crypt plane. However, cell  
789 migration within the crypt plane is simulated by a Monte Carlo approach without  
790 applying explicit energy balance equations. This is possible because inertial forces are  
791 neglected and cell displacement is assumed to be the consequence of cell growth only,  
792 that are common assumptions when modelling cell dynamics in the crypt<sup>59, 63</sup>. To  
793 evaluate the applicability of our model, we have compared simulated cell velocities  
794 with theoretical cell velocities resulting from the total force exerted by neighbouring  
795 cells as the consequence of cell growth and migration<sup>63</sup>. Supplementary Figure S2  
796 shows that the simulated and theoretical velocity is practically the same for a high  
797 percentage (~70%) of cells when they do not change index position in the helix.  
798 During cell relocation in the helix, the balance of forces is maintained only in ~40%  
799 of the cases while for the rest, the simulated velocity is greater than the theoretical  
800 velocity (Supplementary Figure S2). Therefore, a proportion of punctual cell  
801 velocities with our modelling approach could be slightly overestimated.

802

**803 Computational model for the development of a new crypt from the crypt**  
**804 partition process.**

805 The biomechanics of the progression of the initial deformation towards a new  
806 crypt is currently unknown and we have therefore adopted a simple descriptive  
807 geometrical approach. The initial bud is assumed to be formed by the newly generated  
808 cells after division and the surrounding Paneth cells from the original crypt; with  
809 practically no displacement of Paneth cells, the initial spiral is located orthogonally to  
810 the tangent plane to the original stem cell centre. The new crypt is developed from the  
811 bud by proliferation and differentiation of cells that progressively form a new spiral  
812 and helix according to a given final number of crypt cells as previously described<sup>29</sup>.  
813 The final size of the new crypt is assumed to be equal to the size of the primary crypt.

814 We assume that cells in the bud proliferate and generate a new crypt, protruding  
815 from the primary crypt independently of the primary crypt. In the primary crypt the  
816 insertion of the new crypt is represented by a disk of a diameter equal to the  
817 secondary crypt mouth. The new crypt is located orthogonally to the tangent plane to  
818 the central point of the crypt insertion disk and therefore, the lumens of both crypts  
819 are assumed to be connected from the earliest stage (Supplementary Figure S3). Cell  
820 differentiation and proliferation in the primary crypt is not affected by the presence of  
821 the bud so that the primary crypt deals with the area of insertion of the new crypt in  
822 the same way as with no budding regions.

823 Mitotic pressure in the primary crypt forces the upward migration of the  
824 secondary crypt, which simultaneously grows and protrudes out of the primary crypt.  
825 Thus, the growth and migration of the secondary crypt are independent processes. We  
826 assumed that when the secondary crypt reaches its final size its length stops increasing  
827 and cell proliferation forces either cell shedding into the lumen, or cell migration to  
828 any adjacent villus structures or to the walls of the primary crypt, whilst the secondary  
829 crypt has not yet reached the top of the primary crypt. Crypt fission or partition occurs  
830 when the secondary crypt reaches the top of the primary crypt.

831

**832 Stochastic simulation of the growth of the intestinal epithelium by crypt fission**

833 We developed a Monte-Carlo simulation algorithm to simulate the growth of  
834 the intestinal epithelium. The time for the following budding event in a crypt is  
835 generated by randomly sampling from the histogram of the time intervals between

836 budding events in Figure 4A; the specific growth rate is assigned to each crypt by  
837 randomly sampling from the simulated histogram in Figure 5A. Budding times are  
838 used as time steps. At each time step, a new crypt formed by 1 cell is added into the  
839 epithelium and the size of all growing crypts is updated. Crypts stop growing after  
840 reaching their final size. Simulations were started from a single crypt.

841

#### 842 **Statistical Analysis**

843 Growth rates were estimated by lineal regression after the logarithmic  
844 transformation of the dependent variable when required. Median values were  
845 compared by a Wilcoxon-Mann-Whitney test.

846

#### 847 **Acknowledgments**

848 Authors kindly acknowledge the help of Gary Barker with modelling the  
849 behaviour of viscoelastic material.

850

851 **References**

852

- 853 1. L. Cheng, K. Araki, Y. Furuya, T. Matsuoka, K. Mashima, M. Kobayashi and  
854 K. Matsuura, *Med Electron Microsc*, 2000, 33, 165-171.
- 855 2. N. A. Wright and A. Al-Nafussi, *Cell Tissue Kinet*, 1982, 15, 611-621.
- 856 3. A. B. Cairnie and B. H. Millen, *Cell Tissue Kinet*, 1975, 8, 189-196.
- 857 4. N. A. Wright and M. R. Alison, *The biology of epithelial cell populations.*  
858 *Volume 2*, Clarendon Press, Oxford, 1984.
- 859 5. R. M. Clarke, *J Anat*, 1972, 112, 27-33.
- 860 6. C. M. Dekaney, J. J. Fong, R. J. Rigby, P. K. Lund, S. J. Henning and M. A.  
861 Helmuth, *American journal of physiology. Gastrointestinal and liver*  
862 *physiology*, 2007, 293, G1013-1022.
- 863 7. W. H. St Clair and J. W. Osborne, *Cell Tissue Kinet*, 1985, 18, 255-262.
- 864 8. H. S. Wasan, H. S. Park, K. C. Liu, N. K. Mandir, A. Winnett, P. Sasieni, W.  
865 F. Bodmer, R. A. Goodlad and N. A. Wright, *J Pathol*, 1998, 185, 246-255.
- 866 9. N. Barker, R. A. Ridgway, J. H. van Es, M. van de Wetering, H. Begthel, M.  
867 van den Born, E. Danenberg, A. R. Clarke, O. J. Sansom and H. Clevers,  
868 *Nature*, 2009, 457, 608-611.
- 869 10. N. A. Wright, *Int J Exp Pathol*, 2000, 81, 117-143.
- 870 11. W. M. Wong, N. Mandir, R. A. Goodlad, B. C. Wong, S. B. Garcia, S. K. Lam  
871 and N. A. Wright, *Gut*, 2002, 50, 212-217.
- 872 12. A. Humphries and N. A. Wright, *Nat Rev Cancer*, 2008, 8, 415-424.
- 873 13. A. P. Haramis, H. Begthel, M. van den Born, J. van Es, S. Jonkheer, G. J.  
874 Offerhaus and H. Clevers, *Science*, 2004, 303, 1684-1686.
- 875 14. N. Arber and M. Moshkowitz, *Curr Gastroenterol Rep*, 2011, 13, 435-441.
- 876 15. J. Totafurno, M. Bjerknes and H. Cheng, *Biophys J*, 1987, 52, 279-294.
- 877 16. M. Loeffler and B. Grossmann, *J Theor Biol*, 1991, 150, 175-191.
- 878 17. Y. Q. Li, S. A. Roberts, U. Paulus, M. Loeffler and C. S. Potten, *J Cell Sci*,  
879 1994, 107 ( Pt 12), 3271-3279.
- 880 18. M. Loeffler, T. Bratke, U. Paulus, Y. Q. Li and C. S. Potten, *J Theor Biol*,  
881 1997, 186, 41-54.

- 882 19. D. Drasdo, *Phys Rev Lett*, 2000, 84, 4244-4247.
- 883 20. C. M. Edwards and S. J. Chapman, *B Math Biol*, 2007, 69, 1927-1942.
- 884 21. E. Hannezo, J. Prost and J. F. Joanny, *Phys Rev Lett*, 2011, 107, 078104.
- 885 22. M. R. Nelson, D. Howard, O. E. Jensen, J. R. King, F. R. Rose and S. L.  
886 Waters, *Biomech Model Mechanobiol*, 2011, 10, 883-900.
- 887 23. P. Buske, J. Przybilla, M. Loeffler, N. Sachs, T. Sato, H. Clevers and J. Galle,  
888 *FEBS J*, 2012, DOI: 10.1111/j.1742-4658.2012.08646.x.
- 889 24. T. Sato, D. E. Stange, M. Ferrante, R. G. Vries, J. H. Van Es, S. Van den  
890 Brink, W. J. Van Houdt, A. Pronk, J. Van Gorp, P. D. Siersema and H.  
891 Clevers, *Gastroenterology*, 2011, 141, 1762-1772.
- 892 25. T. Sato, R. G. Vries, H. J. Snippert, M. van de Wetering, N. Barker, D. E.  
893 Stange, J. H. van Es, A. Abo, P. Kujala, P. J. Peters and H. Clevers, *Nature*,  
894 2009, 459, 262-U147.
- 895 26. A. Ootani, X. Li, E. Sangiorgi, Q. T. Ho, H. Ueno, S. Toda, H. Sugihara, K.  
896 Fujimoto, I. L. Weissman, M. R. Capecchi and C. J. Kuo, *Nat Med*, 2009, 15,  
897 701-706.
- 898 27. T. Sato, J. H. van Es, H. J. Snippert, D. E. Stange, R. G. Vries, M. van den  
899 Born, N. Barker, N. F. Shroyer, M. van de Wetering and H. Clevers, *Nature*,  
900 2011, 469, 415-+.
- 901 28. A. Durand, B. Donahue, G. Peignon, F. Letourneur, N. Cagnard, C.  
902 Slomianny, C. Perret, N. F. Shroyer and B. Romagnolo, *PNAS USA*, 2012,  
903 109, 8965-8970.
- 904 29. C. Pin, A. J. Watson and S. R. Carding, *Plos One*, 2012, 7, e37115.
- 905 30. H. J. Snippert, A. G. Schepers, J. H. van Es, B. D. Simons and H. Clevers,  
906 *EMBO reports*, 2014, 15, 62-69.
- 907 31. C. S. Potten, *Philosophical Transactions of the Royal Society B-Biological  
908 Sciences*, 1998, 353, 821-830.
- 909 32. A. Hirata, J. Utikal, S. Yamashita, H. Aoki, A. Watanabe, T. Yamamoto, H.  
910 Okano, N. Bardeesy, T. Kunisada, T. Ushijima, A. Hara, R. Jaenisch, K.  
911 Hochedlinger and Y. Yamada, *Development*, 2013, 140, 66-75.
- 912 33. A. Humphries, B. Cereser, L. J. Gay, D. S. Miller, B. Das, A. Gutteridge, G.  
913 Elia, E. Nye, R. Jeffery, R. Poulson, M. R. Novelli, M. Rodriguez-Justo, S. A.  
914 McDonald, N. A. Wright and T. A. Graham, *Proc Natl Acad Sci U S A*, 2013,  
915 110, E2490-2499.
- 916 34. H. Cheng and M. Bjercknes, *Anat Rec*, 1985, 211, 420-426.

- 917 35. J. J. Dehmer, A. P. Garrison, K. E. Speck, C. M. Dekaney, L. Van  
918 Landeghem, X. F. Sun, S. J. Henning and M. A. Helmrath, *Plos One*, 2011, 6.
- 919 36. A. G. Cummins, A. G. Catto-Smith, D. J. Cameron, R. T. Couper, G. P.  
920 Davidson, A. S. Day, P. D. Hammond, D. J. Moore and F. M. Thompson, *J*  
921 *Pediatr Gastroenterol Nutr*, 2008, 47, 153-157.
- 922 37. M. R. Nelson, J. R. King and O. E. Jensen, *Mathematical biosciences*, 2013,  
923 246, 229-241.
- 924 38. S. J. Dunn, A. G. Fletcher, S. J. Chapman, D. J. Gavaghan and J. M. Osborne,  
925 *J Theor Biol*, 2012, 298, 82-91.
- 926 39. D. Drasdo and M. Loeffler, *Nonlinear Analysis-Theory Methods &*  
927 *Applications*, 2001, 47, 245-256.
- 928 40. J. Berlanga-Acosta, R. J. Playford, N. Mandir and R. A. Goodlad, *Gut*, 2001,  
929 48, 803-807.
- 930 41. O. Bashir, A. J. Fitzgerald, J. Berlanga-Acosta, R. J. Playford and R. A.  
931 Goodlad, *Clin Sci (Lond)*, 2003, 105, 323-330.
- 932 42. A. G. Cummins, B. J. Jones and F. M. Thompson, *Digest Dis Sci*, 2006, 51,  
933 718-723.
- 934 43. A. Milicic, L. A. Harrison, R. A. Goodlad, R. G. Hardy, A. M. Nicholson, M.  
935 Presz, O. Sieber, S. Santander, J. H. Pringle, N. Mandir, P. East, J. Obszynska,  
936 S. Sanders, E. Piazuelo, J. Shaw, R. Harrison, I. P. Tomlinson, S. A.  
937 McDonald, N. A. Wright and J. A. Jankowski, *Cancer Res*, 2008, 68, 7760-  
938 7768.
- 939 44. J. K. Fauser, R. P. Donato, J. A. Woenig, S. J. Proctor, A. P. Trotta, P. K.  
940 Grover, G. S. Howarth, I. A. Penttila and A. G. Cummins, *J Pediatr*  
941 *Gastroenterol Nutr*, 2012, 55, 26-31.
- 942 45. P. Andreu, S. Colnot, C. Godard, S. Gad, P. Chafey, M. Niwa-Kawakita, P.  
943 Laurent-Puig, A. Kahn, S. Robine, C. Perret and B. Romagnolo, *Development*,  
944 2005, 132, 1443-1451.
- 945 46. M. E. Rothenberg, Y. Nusse, T. Kalisky, J. J. Lee, P. Dalerba, F. Scheeren, N.  
946 Lobo, S. Kulkarni, S. Sim, D. Qian, P. A. Beachy, P. J. Pasricha, S. R. Quake  
947 and M. F. Clarke, *Gastroenterology*, 2012, 142, 1195-1205 e1196.
- 948 47. S. Roth, P. Franken, A. Sacchetti, A. Kremer, K. Anderson, O. Sansom and R.  
949 Fodde, *Plos One*, 2012, 7, e38965.
- 950 48. J. H. van Es, T. Sato, M. van de Wetering, A. Lyubimova, A. N. Nee, A.  
951 Gregorieff, N. Sasaki, L. Zeinstra, M. van den Born, J. Korving, A. C.  
952 Martens, N. Barker, A. van Oudenaarden and H. Clevers, *Nature cell biology*,  
953 2012, 14, 1099-1104.

- 954 49. S. J. Buczacki, H. I. Zecchini, A. M. Nicholson, R. Russell, L. Vermeulen, R.  
955 Kemp and D. J. Winton, *Nature*, 2013, 495, 65-69.
- 956 50. H. Clevers, *Nature*, 2013, 495, 53-54.
- 957 51. M. Leushacke, A. Ng, J. Galle, M. Loeffler and N. Barker, *Cell*, 2013, 5, 1-8.
- 958 52. H. Miyoshi, R. Ajima, C. T. Luo, T. P. Yamaguchi and T. S. Stappenbeck,  
959 *Science*, 2012, 338, 108-113.
- 960 53. T. Sato, R. G. Vries, H. J. Snippert, M. van de Wetering, N. Barker, D. E.  
961 Stange, J. H. van Es, A. Abo, P. Kujala, P. J. Peters and H. Clevers, *Nature*,  
962 2009, 459, 262-265.
- 963 54. N. Barker, J. H. van Es, J. Kuipers, P. Kujala, M. van den Born, M. Cozijnsen,  
964 A. Haegbarth, J. Korving, H. Begthel, P. J. Peters and H. Clevers, *Nature*,  
965 2007, 449, 1003-U1001.
- 966 55. Q. S. Li, G. Y. Lee, C. N. Ong and C. T. Lim, *Biochem Biophys Res Commun*,  
967 2008, 374, 609-613.
- 968 56. J. L. Hutter and J. Bechhoefer, *Rev Sci Instrum*, 1993, 64, 1868-1873.
- 969 57. F. A. Meineke, C. S. Potten and M. Loeffler, *Cell Proliferat*, 2001, 34, 253-  
970 266.
- 971 58. J. Galle, M. Hoffmann and G. Aust, *J Math Biol*, 2009, 58, 261-283.
- 972 59. P. Buske, J. Galle, N. Barker, G. Aust, H. Clevers and M. Loeffler, *PLoS*  
973 *computational biology*, 2011, 7, e1001045.
- 974 60. J. M. Osborne, A. Walter, S. K. Kershaw, G. R. Mirams, A. G. Fletcher, P.  
975 Pathmanathan, D. Gavaghan, O. E. Jensen, P. K. Maini and H. M. Byrne,  
976 *Philos T Roy Soc A*, 2010, 368, 5013-5028.
- 977 61. M. Loeffler, R. Stein, H. E. Wichmann, C. S. Potten, P. Kaur and S.  
978 Chwalinski, *Cell Tissue Kinet*, 1986, 19, 627-645.
- 979 62. M. Loeffler, C. S. Potten, U. Paulus, J. Glatzer and S. Chwalinski, *Cell Tissue*  
980 *Kinet*, 1988, 21, 247-258.
- 981 63. J. Pitt-Francis, P. Pathmanathan, M. O. Bernabeu, R. Bordas, J. Cooper, A. G.  
982 Fletcher, G. R. Mirams, P. Murray, J. M. Osborne, A. Walter, S. J. Chapman,  
983 A. Garny, I. M. M. van Leeuwen, P. K. Maini, B. Rodriguez, S. L. Waters, J.  
984 P. Whiteley, H. M. Byrne and D. J. Gavaghan, *Comput Phys Commun*, 2009,  
985 180, 2452-2471.

986

987 **Figure Legends**

988

989 **Figure 1.** Fluorescent microscopy of small intestinal organoids undergoing budding  
990 events. Lgr5+ stem cells are labelled in green. Lysozyme granules in Paneth cells are  
991 in red and cell nuclei in blue. Yellow arrows point at Paneth and stem cells  
992 intermingling at the base of the crypts. Red arrows indicate the initiation of buds in  
993 regions where Paneth cells are located. Green arrows point at stem cells located in  
994 between Paneth cells.

995 **Figure 2.** Crypt fission in cultured murine small intestinal organoids. Budding is  
996 initiated in areas rich in Paneth cells (asterisk).

997 **Figure 3.** (A) Comparison of the Young's modulus measured by Atomic Force  
998 Microscopy (AFM) of Lgr5-eGFP positive stem cells (red lines) and Paneth cells  
999 identified visually as non-fluorescent large granular cells (black lines). The Young's  
1000 modulus reflects cell stiffness. (B) AFM force approach and retract curves showing  
1001 hysteresis characteristic to viscous material. Colour codes as in 3A.

1002 **Figure 4.** Comparison between fission measurements in simulated crypts and in  
1003 cultured organoids: (A) Observed (black bars; n=22 initial crypts) and simulated (red  
1004 bars; n=30-40 initial crypts simulated during 12 days for each tested value of  $\alpha$ )  
1005 distributions for the time interval between successive budding processes per crypt.  
1006 Plots show the results obtained with twelve values of the parameter  $\alpha$ , from 0.1 to 2,  
1007 which controls the force required to deform Paneth cells. (B) Square difference  
1008 between the observed and simulated frequencies plotted in Figure 4A; the smallest  
1009 difference was detected with  $\alpha = 1.3$ . (C) Simulated probability of budding -within a  
1010 12 days period- of stem cells clusters surrounded by Paneth cells with several values  
1011 for the parameter  $\alpha$  and for cluster sizes of 1 (●), 2 (◇), 3 (+) and 4 (○) stem cells. (D)  
1012 Percentage of clusters of stem cells surrounded by Paneth cells of size of 1 (●), 2 (◇),  
1013 3 (+) and 4 (○) stem cells in simulated crypts. (E-H) Schematic representation of the  
1014 location of the cell centres on the ring of the crypt formed by stem, S, and Paneth, P,  
1015 cells when (E) all cells are deformable stem cells; (F) Paneth and stem cells have the  
1016 same viscoelastic behaviour and (G) Paneth cells are more resistant to deformation  
1017 ( $\alpha=1.3$ ) than stem cells. The simulated location of cell centres occurs over a period of  
1018 20 days. For all hypotheses the duration of the stem cell division cycle is a normal  
1019 distributed random variable with a mean value of 21.5 h and standard deviation of  
1020 2.15 h. Stem cells divide asynchronously. (H) Location of cell centres (dots) and cell  
1021 boundaries (lines) at the beginning of the division cycle (discontinuous lines) of a



1022 stem cell (marked with an asterisk) surrounded by Paneth cells and ~21 h later  
1023 immediately before division (continuous lines) under the hypothesis that Paneth cells  
1024 are more resistance to deformation ( $\alpha=1.3$ ).

1025

1026 **Figure 5.** (A) Observed (black bars;  $n=17$ ) and simulated (red bars;  $n=89$ )  
1027 distributions for the for the specific growth rate of the crypt length. (B) Observed  
1028 (black) and simulated (red) migration curves of the secondary crypt along the length  
1029 of the primary crypt expressed in percentage.

1030

1031 **Figure 6.** Appearance of a secondary crypt completely developed at the base of the  
1032 original crypt without migrating upwards and which replaces the original crypt.

1033

1034 **Figure 7.** Simulated growth of the new crypt and migration along the original crypt:  
1035 (A) Simulated distributions of the time for the secondary crypt to reach its final size  
1036 and (B) to reach the top of the original crypt. (C) Distribution of the position of the  
1037 secondary crypt when reaching the final size and (D) of the size -number of cells- of  
1038 the secondary crypt when reaching the top of the original crypt.

1039

1040 **Figure 8.** Average proportions of each cell type during crypt fission. A) Proportion of  
1041 stem and secretory cells and B) of proliferative cells and absorptive progenitors per  
1042 crypt.

1043

1044 **Figure 9.** Predicting growth of the intestinal epithelium by crypt fission. The  
1045 predicted number of crypts and cells in the newly formed tissue assumes that budding  
1046 and fission always take place in a crypt when a stem cell is surrounded by Paneth  
1047 cells.

1048

1049 **Figure 10.** Geometry of the viscoelastic behavior of cells within the crypt. The  
1050 deformation of the external side of the cell can be monitored by measuring the  
1051 deformation of either the central vertical,  $i$ , or central horizontal,  $ii$ , axis. The pressure  
1052 per unit length,  $P$ , derives from the difference between cell size and available space  
1053 and it is uniformly applied to the external edge of a cell of width equal to  $2R$ . The  
1054 length of the cell external edge is equal to  $L$ .  $v_y$  is the velocity of the flow in the  $Y$   
1055 direction.

1056

1057 **Supplementary data**

1058

1059 **Table S1.** Individual based model parameters

1060

1061 **Figure S1.** Frequency of cell velocities (cell positions/h) along the crypt during index  
1062 reassignment process, i.e. moving to the ring immediately above (blue columns), and  
1063 during time intervals in which cells do not change rings (red columns). Velocities are  
1064 estimated in the three-dimensional space (A) as well as in each of the dimensions, Z  
1065 (B), X (C) and Y (D). Velocities were estimated from 14,000 cells located in the  
1066 upper half of a simulated crypt during one week. Numbers represent the average  
1067 velocities and their standard errors for each group of cells according to colour.

1068

1069 **Figure S2.** Comparison of the theoretical velocity derived from the balance of forces  
1070 within the crypt and the simulated velocity in our model. The difference between the  
1071 theoretical and simulated velocity was measured in 40,000 cells evolving in a  
1072 simulated crypt during one week. Blue columns represent velocity frequencies for  
1073 cells undertaking index reassignment and therefore moving to the ring immediately  
1074 above, while red columns are for cells that do not change ring. Numbers represent the  
1075 average velocities for each group of cells according to colour.

1076

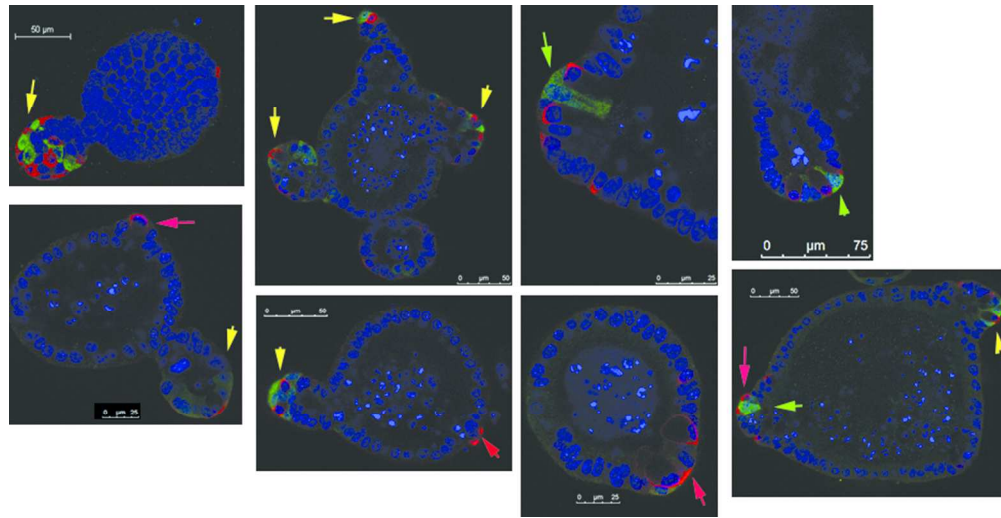
1077 **Figure S3.** Longitudinal view of a simulated fission event. The white arrow marks the  
1078 initial location of the bud in the primary crypt at the time of fission initiation. The bud  
1079 grows into a crypt that migrates upwards the primary crypt in the following days. The  
1080 lumen (red) of both crypts is connected during this process.

1081

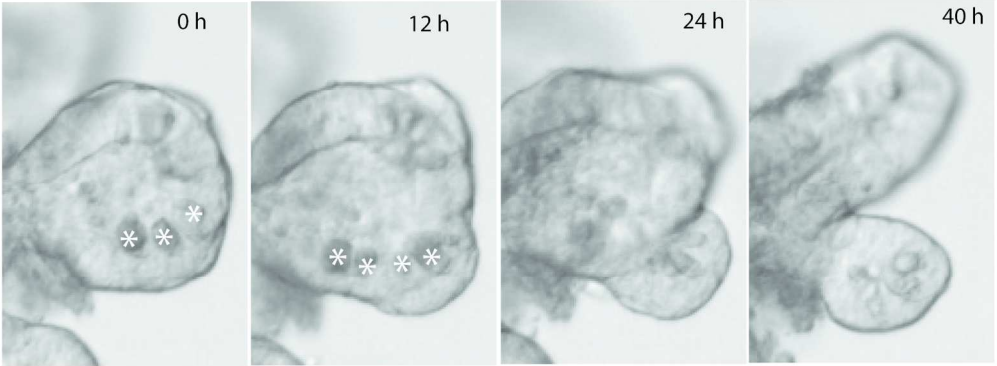
1082 **Video S1.** Simulation of a crypt fission event. Cells are represented by spherical  
1083 shapes unrelated to the modelled cell shape.

1084

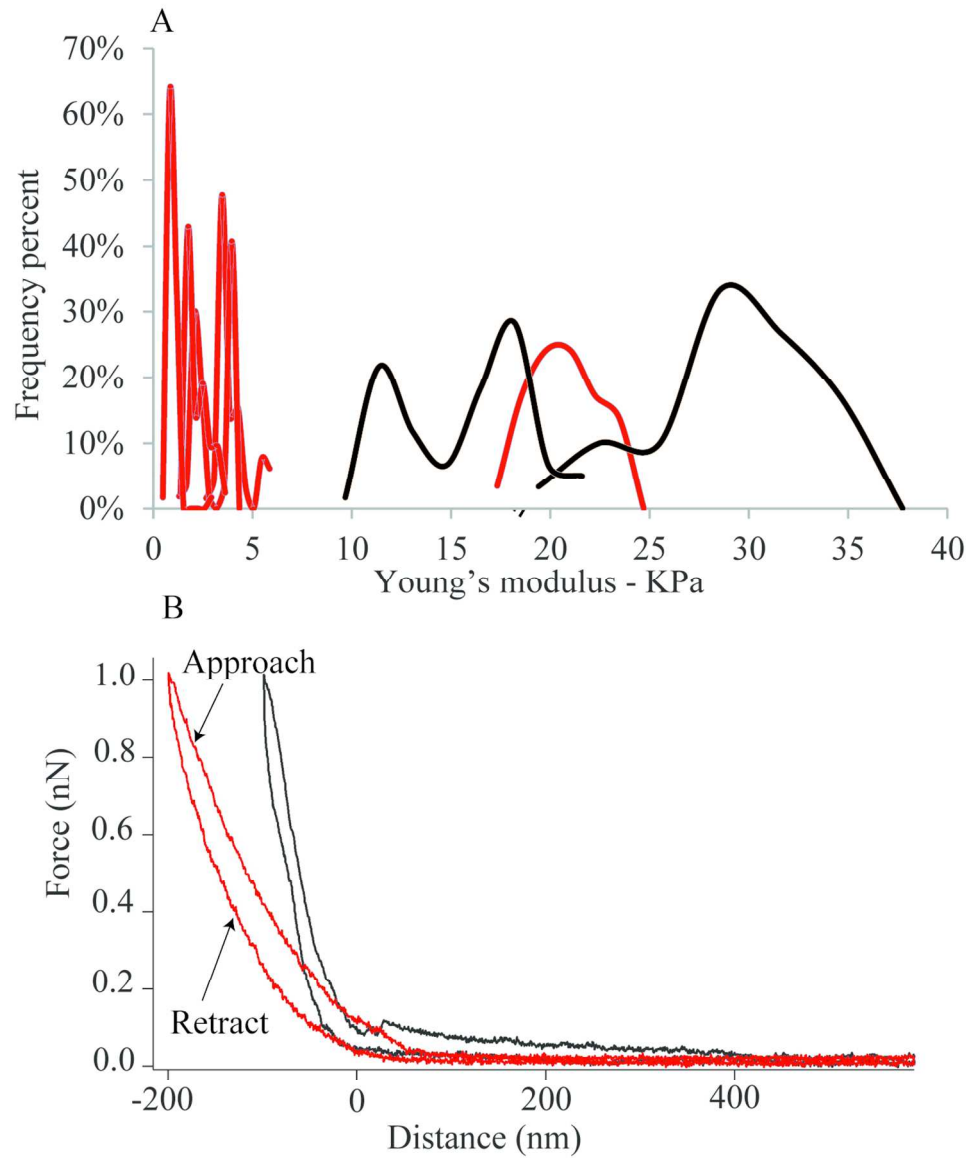
1085 **Video S2.** Simulation of a crypt fission event coupled with the observation of a crypt  
1086 undergoing fission in a cultured organoid - period of observation is 1.2 days. Cells are  
1087 represented by spherical shapes unrelated to the modelled cell shape.



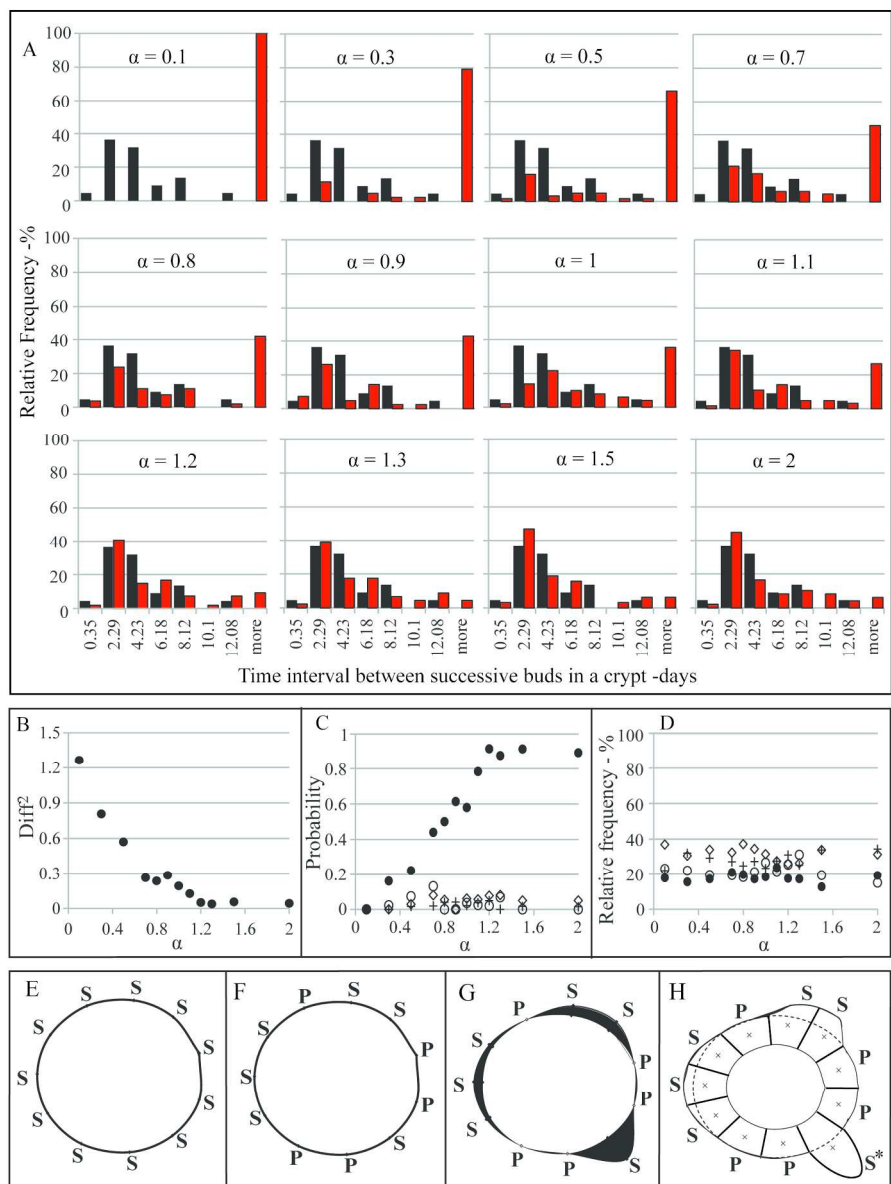
329x168mm (72 x 72 DPI)



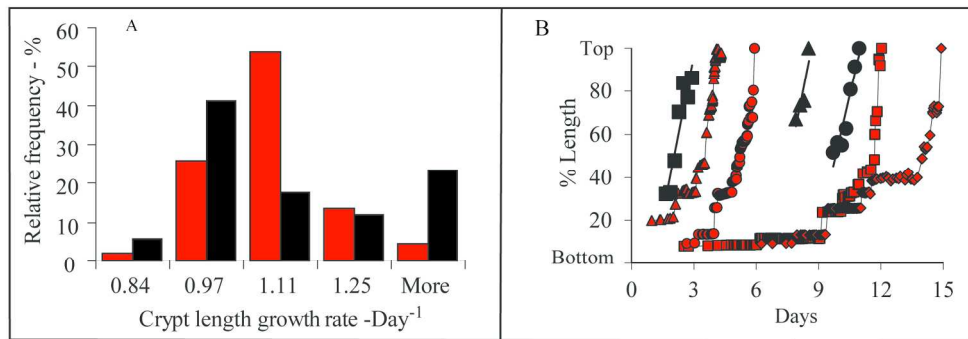
179x66mm (300 x 300 DPI)



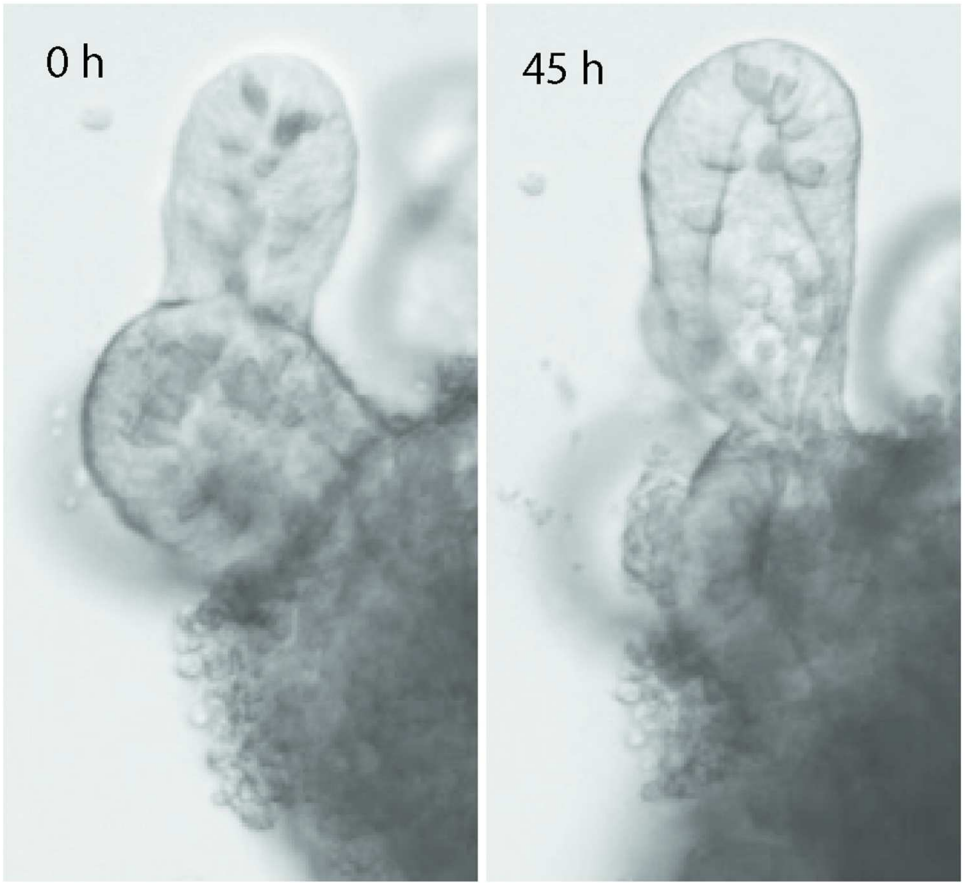
123x148mm (300 x 300 DPI)



182x243mm (300 x 300 DPI)

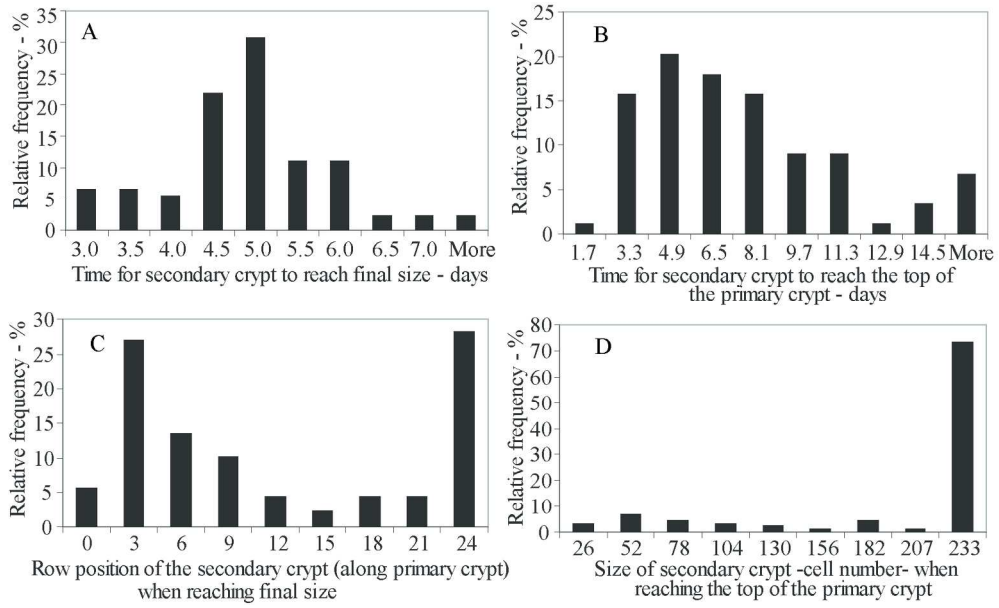


185x67mm (300 x 300 DPI)

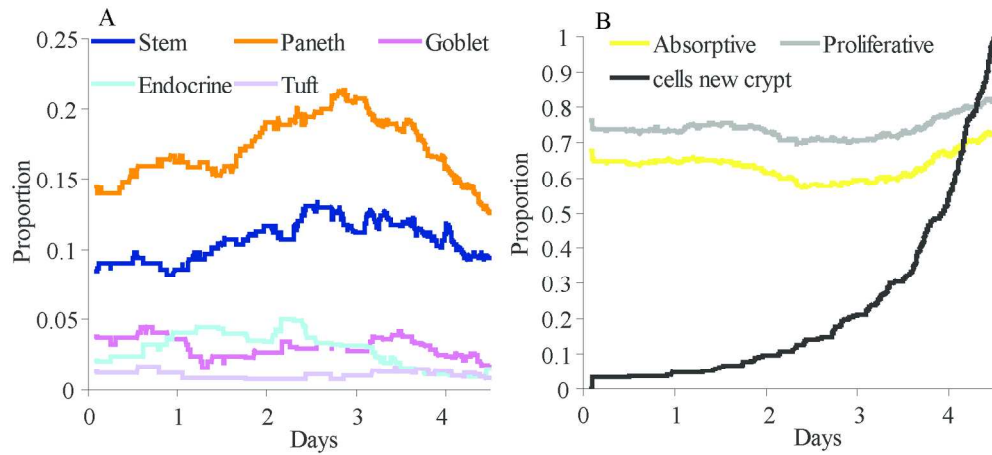


90x82mm (300 x 300 DPI)

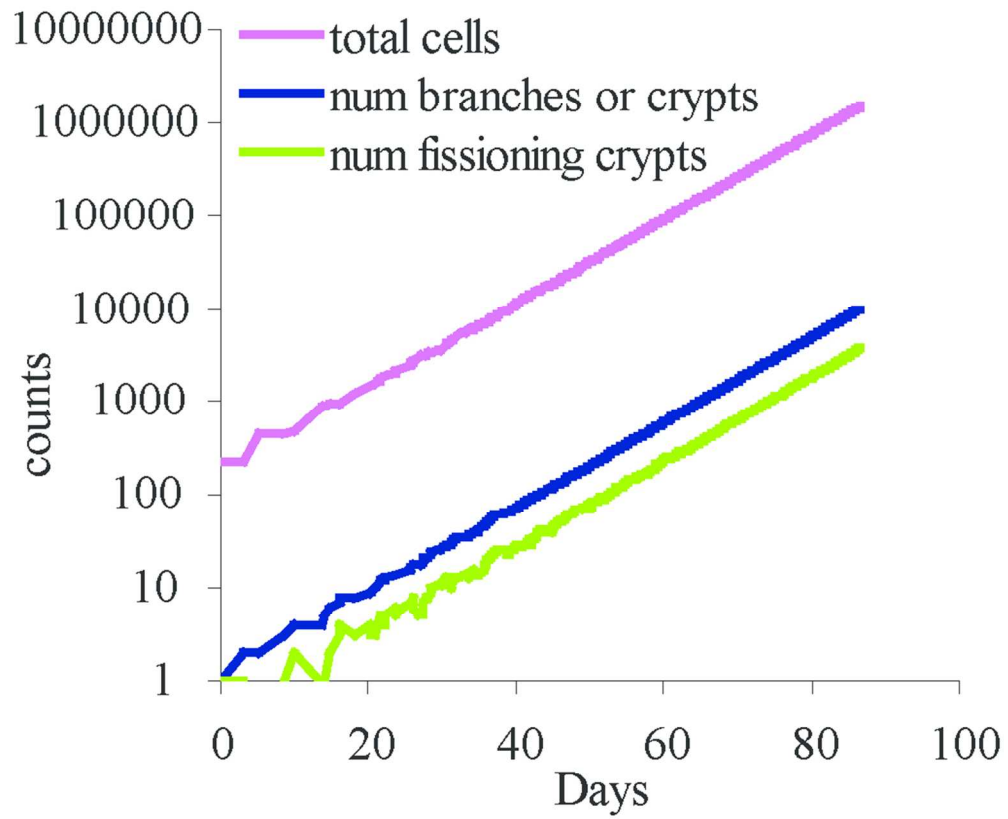




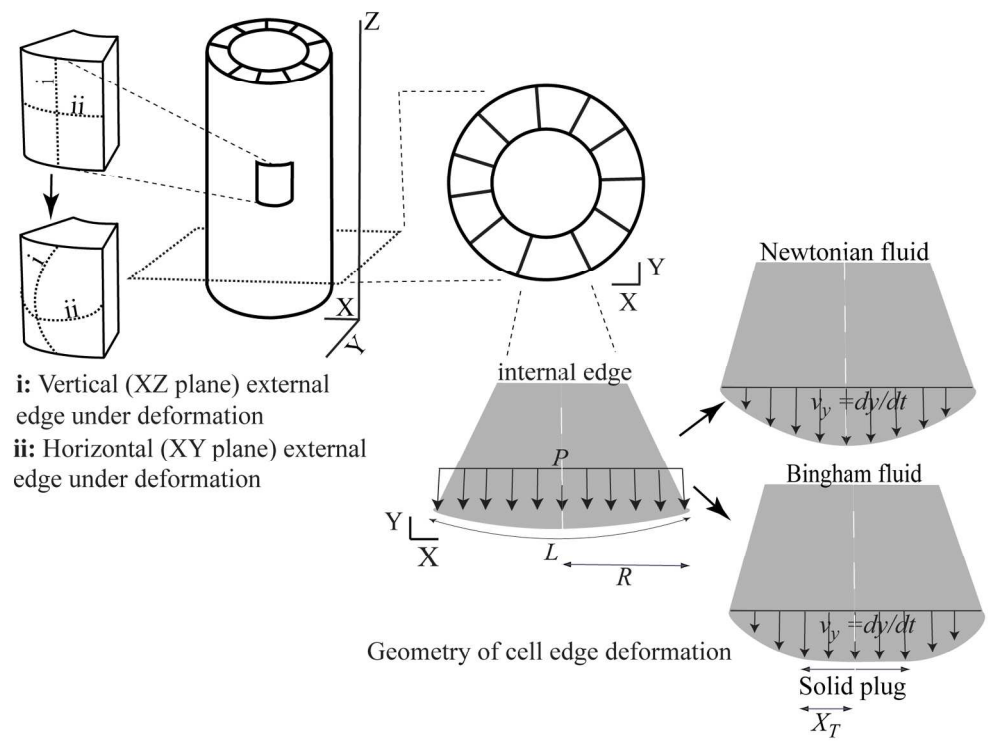
180x109mm (300 x 300 DPI)



172x78mm (300 x 300 DPI)



87x71mm (300 x 300 DPI)



163x123mm (300 x 300 DPI)

**Table S1.** Individual based model parameters

Parameter	Value	source	definition
$n_{cells}$	235	data <sup>29</sup>	Number of cells in the crypt
$n_{spiral}$	33	data <sup>29</sup>	Number of Paneth and Stem cells in the stem cell niche
$Diff_{Secr}$	>50%	data <sup>29</sup>	Percentage of secretory neighbouring cells that inhibit differentiation into secretory lineage
$D_c$	$-5.7091 N_d + 21.449$	data <sup>29, 62</sup>	Duration of division cycle (hours). $N_d$ is the number of undertaken divisions by the cell: its value is fixed to 0 for stem cells and for transit cells the maximum value is 2.
$n$	6	data <sup>29</sup>	Maximum number of division cycles in transit amplifying cells
$R_{av}$	5	data	Average cell radius at birth ( $\mu\text{m}$ )
$r_{av}$	$\frac{\pi R_{av}^2}{D_c}$	data	Average growth rate of the surface area of cells ( $\mu\text{m}^2 \text{h}^{-1}$ )
$\alpha$	1.3	data	Parameter governing the shear stress threshold in Paneth cells

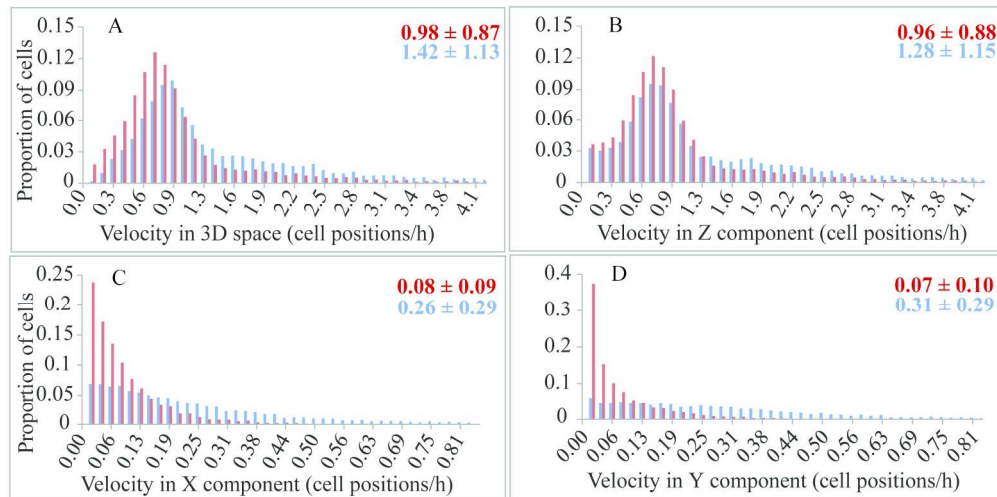


Figure S1. Frequency of cell velocities (cell positions/h) along the crypt during index reassignment process, i.e. moving to the ring immediately above (blue columns), and during time intervals in which cells do not change rings (red columns). Velocities are estimated in the three-dimensional space (A) as well as in each of the dimensions, Z (B), X (C) and Y (D). Velocities were estimated from 14.000 cells located in the upper half of a simulated crypt during one week. Numbers represent the average velocities and their standard errors for each group of cells according to colour.

193x96mm (300 x 300 DPI)

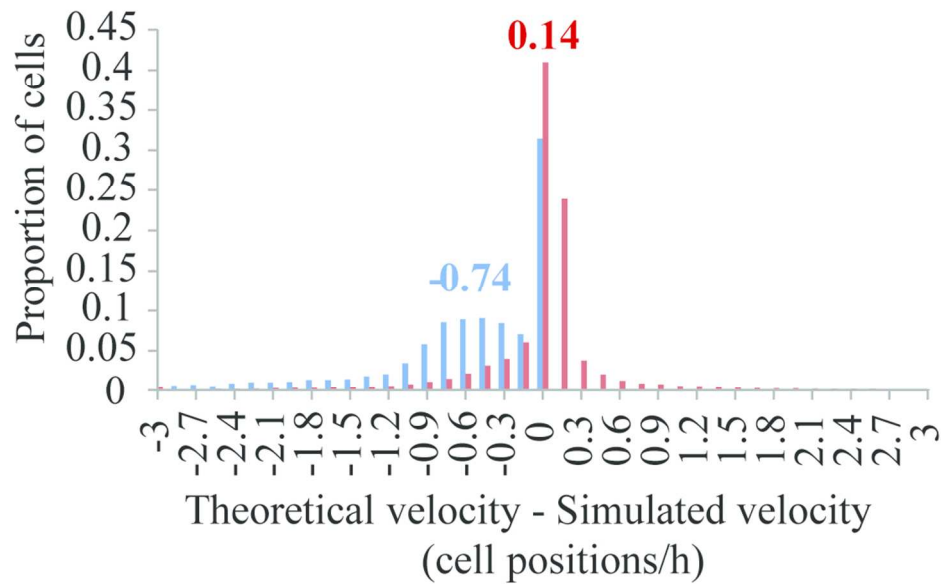


Figure S2. Comparison of the theoretical velocity derived from the balance of forces within the crypt and the simulated velocity in our model. The difference between the theoretical and simulated velocity was measured in 40,000 cells evolving in a simulated crypt during one week. Blue columns represent velocity frequencies for cells undertaking index reassignment and therefore moving to the ring immediately above, while red columns are for cells that do not change ring. Numbers represent the average velocities for each group of cells according to colour.

101x61mm (300 x 300 DPI)



Figure S3. Longitudinal view of a simulated fission event. The white arrow marks the initial location of the bud in the primary crypt at the time of fission initiation. The bud grows into a crypt that migrates upwards the primary crypt in the following days. The lumen (red) of both crypts is connected during this process.  
185x76mm (300 x 300 DPI)